JBC RESEARCH ARTICLE

Integrated multiomics analysis identifies molecular landscape perturbations during hyperammonemia in skeletal muscle and myotubes

Received for publication, May 3, 2021, and in revised form, July 16, 2021 Published, Papers in Press, July 31, 2021,
https://doi.org/10.1016/j.jbc.2021.101023

Nicole Welch[1,2], **Shashi Shekhar Singh**[1], **Avinash Kumar**[1], **Saugato Rahman Dhruba**[3], **Saurabh Mishra**[1], **Jinendiran Sekar**[1], **Annette Bellar**[1], **Amy H. Attaway**[1,4], **Aruna Chelluboyina**[1], **Belinda B. Willard**[5], **Ling Li**[5], **Zhiguang Huo**[6], **Sadashiva S. Karnik**[7], **Karyn Esser**[8], **Michelle S. Longworth**[1], **Yatrik M. Shah**[9], **Gangarao Davuluri**[10], **Ranadip Pal**[3,*], and **Srinivasan Dasarathy**[1,2,*]

From the [1]*Department of Inflammation & Immunity, Lerner Research Institute,* [2]*Department of Gastroenterology and Hepatology, Cleveland Clinic, Cleveland, Ohio, USA;* [3]*Department of Electrical and Computer Engineering, Texas Tech University, Lubbock, Texas, USA;* [4]*Department of Pulmonary Medicine,* [5]*Proteomics Research Core Services, Lerner Research Institute, Cleveland Clinic, Cleveland, Ohio, USA;* [6]*Department of Biostatistics, College of Public Health and Health Profession, University of Florida, Gainesville, Florida, USA;* [7]*Department of Cardiovascular and Metabolic Sciences, Lerner Research Institute, Cleveland Clinic, Cleveland, Ohio, USA;* [8]*Department of Physiology and Functional Genomics, College of Medicine, University of Florida, Gainesville, Florida, USA;* [9]*Department of Molecular & Integrative Physiology and Department of Gastroenterology, University of Michigan, Ann Arbor, Michigan, USA;* [10]*Integrated Physiology and Molecular Metabolism, Pennington Biomedical Research Center, Baton Rouge, Louisiana, USA*

Edited by John Denu

Ammonia is a cytotoxic molecule generated during normal cellular functions. Dysregulated ammonia metabolism, which is evident in many chronic diseases such as liver cirrhosis, heart failure, and chronic obstructive pulmonary disease, initiates a hyperammonemic stress response in tissues including skeletal muscle and in myotubes. Perturbations in levels of specific regulatory molecules have been reported, but the global responses to hyperammonemia are unclear. In this study, we used a multiomics approach to vertically integrate unbiased data generated using an assay for transposase-accessible chromatin with high-throughput sequencing, RNA-Seq, and proteomics. We then horizontally integrated these data across different models of hyperammonemia, including myotubes and mouse and human muscle tissues. Changes in chromatin accessibility and/or expression of genes resulted in distinct clusters of temporal molecular changes including transient, persistent, and delayed responses during hyperammonemia in myotubes. Known responses to hyperammonemia, including mitochondrial and oxidative dysfunction, protein homeostasis disruption, and oxidative stress pathway activation, were enriched in our datasets. During hyperammonemia, pathways that impact skeletal muscle structure and function that were consistently enriched were those that contribute to mitochondrial dysfunction, oxidative stress, and senescence. We made several novel observations, including an enrichment in antiapoptotic B-cell leukemia/lymphoma 2 family protein expression, increased calcium flux, and increased protein glycosylation in myotubes and muscle tissue upon hyperammonemia. Critical molecules in these pathways were validated experimentally. Human skeletal muscle from patients with cirrhosis displayed similar responses, establishing translational relevance. These data demonstrate complex molecular interactions during adaptive and maladaptive responses during the cellular stress response to hyperammonemia.

Essential cellular functions, including amino acid catabolism, purine breakdown, and gut bacterial metabolism in humans, generate cytotoxic ammonia (1–3). The primary mode of ammonia disposal is *via* hepatocyte ureagenesis (1, 2). Dysregulated ammonia metabolism occurs in a number of chronic diseases, and the consequent hyperammonemia causes dysfunction in multiple organs (4). During hyperammonemia, skeletal muscle becomes a major organ for ammonia uptake (5, 6). Consequences of skeletal muscle hyperammonemia include activation of inhibitor of nuclear factor kappa B kinase subunit beta and p65–NFκB and a sarcopenic phenotype (7); more recently, a hyperammonemic stress response (HASR) with decreased protein synthesis and increased autophagy flux has been reported (7–10). Accelerated degradation of β-catenin with impaired ribosomal biogenesis and the reduced expression of a number of ribosomal proteins has also been reported (11). Metabolic perturbations during hyperammonemia include loss of tricarboxylic acid cycle intermediates, or cataplerosis, impaired mitochondrial oxidative function, and changes in amino acid metabolic pathways (12–15). These data show specific metabolic and molecular responses during HASR, but the global molecular changes that can provide an understanding of interacting cellular pathways have not been comprehensively analyzed. Our approach also has broad applications in studies of tissue and cellular

---

* For correspondence: Srinivasan Dasarathy, dasaras@ccf.org; Ranadip Pal, Ranadip.pal@ttu.edu.

responses to different stressors. Global regulatory responses in cellular systems and tissues, *in vivo*, are increasingly being studied using unbiased systems biology approaches (16–18). Notably, systems biology approaches have been used to understand regulation of cellular responses that contribute to human diseases, such as chronic kidney disease, aortic valve disease, and cardiac remodeling (19–22), through approaches that involve vertical integration of the regulome, including patterns of differentially accessible chromatin (DAC), differentially expressed genes (DEG), and differentially expressed proteins (DEPs) (18, 23, 24). However, no studies have specifically integrated chromatin accessibility, transcription, and proteomics data from cellular models, mouse models, and human patients, and we chose hyperammonemia as a model to validate such an approach.

We used both *vertical integration*, or integration of data using the framework of the central dogma—from DNA to RNA to protein, and *horizontal integration*, or the direct comparison of transcriptomics and proteomics in myotubes and mouse and human skeletal muscle. In the present studies, we performed assay for transposase-accessible chromatin with high-throughput sequencing (ATAC-Seq), next-generation RNA-Seq, and quantitative proteomics in a well-characterized murine myotube model of hyperammonemia that reproduces the biochemical, molecular, and phenotypic responses observed in skeletal muscle from human patients with cirrhosis and hyperammonemia (7, 8, 15). The distinct patterns of change identified in our analyses were classified as early transient change, pseudosilent change, late change, and persistent change. We interpret the early transient change to be an "adaptive phase" of hyperammonemia when significant changes occur in the chromatin accessibility, transcriptome, and proteome at 3 h (3hAm), but these changes return to baseline, or untreated (UnT), levels at 24 h (24hAm). Pseudosilent change was interpreted as the cellular responses that attempt to drive expression in one direction (increase or decrease) initially that later is sensed to be a progression toward adverse outcomes. Consequently, the expression of the genes is reversed in an attempt to restore homeostasis. Late changes are a failure of early adaptive processes to return the molecular responses to the baseline homeostatic state and may represent a "maladaptive phase" of responses that occurs with longer ammonia exposure. Persistent changes are perturbations in molecular pathways/molecules that are unable to return to baseline because of the continued stress and may be a maladaptive response or a persistent attempt at adaptive response. Our data also show that adaptive, maladaptive, and restoration to homeostasis or progression to cell death responses occur across multiple pathways that share molecules.

We established the physiological relevance of these cellular responses by performing RNA-Seq and quantitative proteomic analyses of skeletal muscle from a mouse model of hyperammonemia (25). Finally, we identified gene expression changes in skeletal muscle tissue from human patients with cirrhosis, a major chronic liver disease characterized by hyperammonemia to determine translational congruity of our unbiased findings. Interestingly, we found that while changes in expression patterns of specific genes were not always conserved among the experimental systems used, similar pathways were altered. Consistent changes were noted in calcium, hypoxia-inducible factor 1-alpha (HIF1α), senescence, and transforming growth factor β (TGF-β) signaling and protein synthesis pathways over time and across different species. These data identify a novel link between HIF1α and senescence pathways during hyperammonemia. Our cellular studies also identified temporal changes in specific pathways and provide insight into early adaptive events that may contribute to the maladaptive phase of HASR. These data suggest that our preclinical models are translationally relevant and can be used to identify mechanistic therapeutic targets.

Results

A schematic of our approach of vertical and horizontal integration, clusters of global responses, and establishing translational relevance in human samples with experimental validation of critical findings is shown in Figure 1.

Proteomics analyses showed temporally clustered responses in myotubes during hyperammonemia

Cellular functions are mediated *via* changes in protein expression, but less is known about the interactions and contributions of these alterations to overall cellular responses. Modifications in protein expression contribute to both adaptive and maladaptive responses. Therefore, a proteome-wide analysis was first performed to identify early and late changes to integrate overall responses to HASR. Proteomics analyses in C2C12 myotubes showed that the most DEP were found at 24hAm *versus* UnT (n = 226) and 24hAm *versus* 3hAm (n = 95) with fewer DEP found in the 3hAm *versus* UnT (n = 53) treatment comparison (Fig. 2, *A* and *B*). We defined four clusters of DEP based on their pattern of change: early transient change (significant expression differences at 3hAm *versus* UnT with or without a significant change at 24hAm *versus* 3hAm but not at 24hAm *versus* UnT), pseudosilent change (change at 24hAm *versus* 3hAm, but neither the expression at 24hAm or 3hAm was different from UnT), late change (change only at 24hAm *versus* UnT with or without a significant change at 24hAm *versus* 3hAm, but no difference between 3hAm and UnT), and persistent change (both 3hAm and 24hAm were different from UnT). Changes in the clusters suggest a temporal pattern of cellular responses. The physiological significance of the alterations in the pseudosilent cluster is currently unclear but may represent active adaptive responses over time (Fig. S1, *A*–*D*). Cluster analyses of the proteomics expression patterns showed that the late change cluster had the most DEP (n = 323), with fewer DEP in the early transient (n = 60) and persistent change (n = 37) clusters. We noted a high level of concordance between different functional enrichment analyses (ingenuity pathway analysis [IPA], Gene Ontology [GO], and Kyoto Encyclopedia of Genes and Genomes) (Fig. S2, *A* and *B*), indicating that interpretation of our data was similar irrespective of the approach/algorithm used. In both the late change and persistent change clusters in

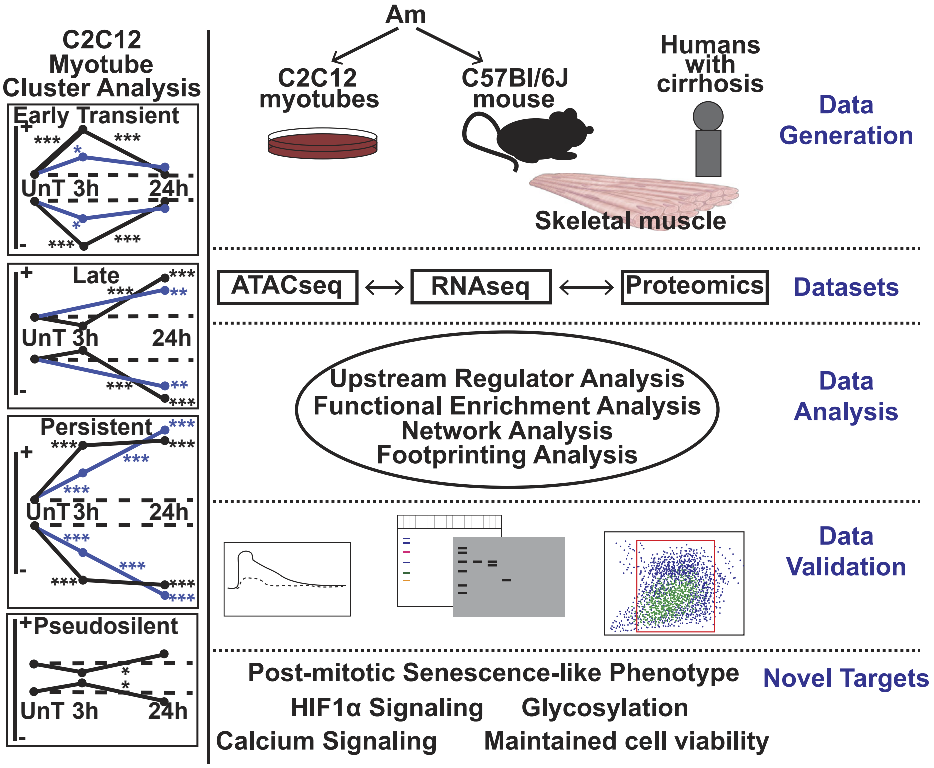

Figure 1. Graphical summary. Data were generated from C2C12 myotubes and skeletal muscle from mice treated with 10 mM ammonium acetate (Am) or PBS and from human patients with cirrhosis and controls. Datasets from cells and tissues were created using ATAC-Seq, RNA-Seq, and quantitative proteomics. As shown on the *left panels*, datasets from C2C12 myotubes were separated into clusters of early transient (increase or decrease in accessibility/expression at 3hAm with a return to baseline [UnT] expression at 24hAm), late (increase or decrease in accessibility/expression at 24hAm *versus* 3hAm and/or 24hAm *versus* UnT), persistent (increase or decrease in accessibility/expression at both 3hAm and 24hAm *versus* UnT), and pseudosilent (increase or decrease in accessibility/expression only at 24hAm *versus* 3hAm but not with either Am treatment *versus* UnT) change groups. Footprinting analyses from ATAC-Seq were also parsed into the same clusters. Functional enrichment analyses were performed on myotube dataset clusters and mouse and human datasets. Validation experiments were performed using real-time PCR, immunoblots, flow cytometry, calcium flux, and transcription factor array. Novel processes as targets emerged including postmitotic senescence-like phenotype, calcium signaling, and HIF1α signaling. Am, ammonium acetate; ATAC-Seq, assay for transposase-accessible chromatin with high-throughput sequencing; HIF1α, hypoxia-inducible factor 1-alpha; UnT, untreated.

the proteomics dataset, the protein synthesis regulatory pathways (including mammalian target of rapamycin [mTOR] and pP70S6k signaling) were significantly enriched (Fig. 2, *C–E*) and are consistent with our previous report of impaired mTOR complex 1 signaling during hyperammonemia (9, 11, 15). Also, consistent with our published data on hyperammonemia (9, 10, 15, 26), oxidative stress response, AMP-activated protein kinase (AMPK) signaling, tricarboxylic acid cycle, and glycolysis pathways were among the pathways enriched in the late change cluster in the proteomics dataset in myotubes. We have previously reported an increase in eukaryotic initiation factor-2 α (eIF2α) phosphorylation during HASR (10). eIF2 signaling and calcium signaling were the most enriched pathways in the late change dataset. Other pathways, including HIF1α signaling and apoptosis were also enriched in the late change myotube proteomics cluster. Changes in components of these pathways have been reported by us and others during hyperammonemia (10, 27–29) and in our experimental studies that showed increased calcium flux in myotubes with ammonia exposure (Fig. 2*F*). These observations are consistent with reports by others of ammonia-induced changes in calcium signaling that mediate oxidative stress responses in astrocytes (30, 31). To validate our proteomics data, we chose highly DEPs, which were included in the pathways described previously, and performed immunoblotting on lysates from treated or UnT myotubes over the 24-h time course. We then experimentally validated expression of critical skeletal muscle regulatory and structural proteins on immunoblots. Consistent with our proteomics data, we noted lower expression of myosin heavy chain at 3hAm *versus* UnT and lower expression of caveolin-3 at 24hAm/3hAm *versus* UnT. We also observed higher expression of NLR family, apoptosis inhibiting protein 1 at 24hAm *versus* UnT and of B-cell leukemia/lymphoma 2 (Bcl2) at 24hAm *versus* UnT/3hAm (Fig. 2*G*). We then evaluated cell viability and apoptosis markers as a measure of overall cellular functional response. Even though others have reported an increase in apoptosis during hyperammonemia (29, 32), our published (8) and experimental observations show unaltered cell viability during hyperammonemia (Fig. 2*H*). These observations were consistent with increased expression of antiapoptotic molecule, Bcl2 (Fig. 2*G*), and unaltered apoptosis markers, including cleaved caspase 3, poly(ADP-ribose) polymerase 1 (PARP1) expression (Fig. 2*H*), and annexin V in UnT as well as 3hAm- and 24hAm-treated myotubes (Fig. S3). Immunoblots for HIF1α in myotubes showed stabilization at 24hAm

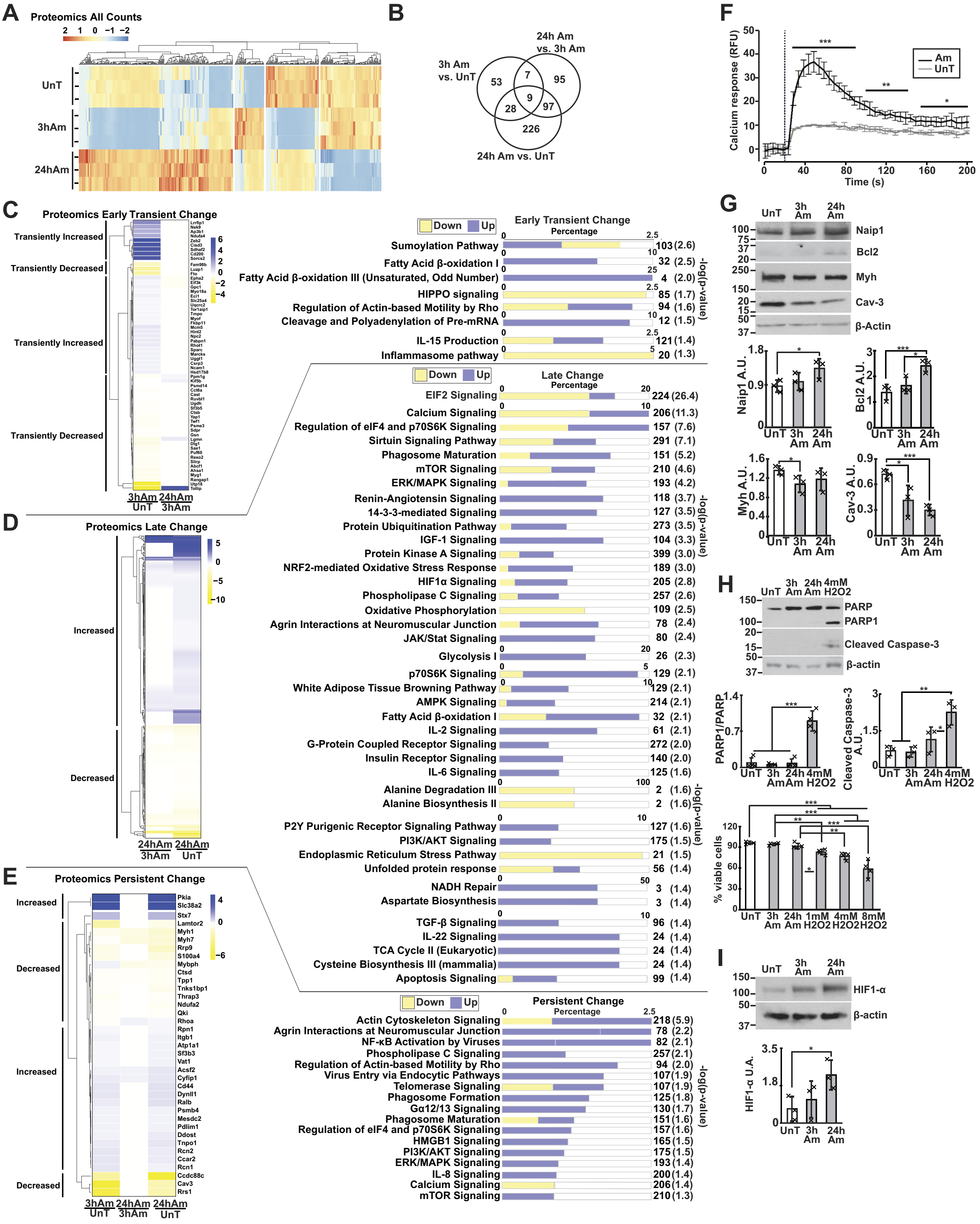

Figure 2. Proteomic landscape in differentiated murine myotubes during hyperammonemia. *A*, heat map of differentially expressed proteins (DEP) in myotubes that were either untreated (UnT) or treated with 3 h or 24 h of 10 mM ammonium acetate (Am). *B*, Venn diagram of unique DEP in UnT myotubes or those treated with 3hAm and 24hAm and analyzed for differential expression using the following comparisons: 3hAm *versus* UnT, 24hAm *versus* 3hAm, and 24hAm *versus* UnT. *C*, heat map of myotube DEP with significant increase or decrease in expression at 3hAm with a return to baseline (UnT) expression at 24 h, termed early transient change. *Stacked bar chart* showing manually curated canonical pathways that are significantly enriched in the early transient

compared with UnT controls, consistent with our unbiased data analyses (Fig. 2*I*). Thus, our unbiased proteomics data show that clusters of responses to hyperammonemia involve a global reprogramming that follows a distinct temporal course with maintained cell viability.

Global transcriptomics responses showed multiple pathway enrichments during hyperammonemia in myotubes

We then evaluated if transcriptomic responses in myotubes followed the temporal and expression patterns that were identified on the proteomics analyses. In addition to shared genes, a number of unique DEG in both the 24hAm *versus* UnT (n = 1082) and 24hAm *versus* 3hAm (n = 1284) treatment comparisons were noted (Fig. 3). In contrast, there were few (n = 3) unique DEG at 3hAm *versus* UnT (Fig. 3, *A* and *B*). Consistent with our observations in the proteomics cluster analyses, the largest number of DEG (n = 2795) in the RNA-Seq dataset was in the late change cluster (Fig. 3*B*). Functional enrichment analysis was then performed in the different clusters in the RNA-Seq dataset (Fig. 3, *C*–*E*, Figs. S1 and S4, *A* and *B*). In the pseudosilent cluster, oxidative phosphorylation, sirtuin signaling, and mRNA translational components were among the significantly enriched pathways (Fig. S1*C*). In the late change cluster, enrichment of HIF1α signaling, senescence, and metabolic regulation pathways (Fig. 3*D*) was observed. AMPK, interleukin-6, and death receptor signaling pathway components were significantly altered in both late and pseudosilent clusters. Confirmatory real-time PCR performed for select genes showed results consistent with the RNA-Seq DEG, including an increase in *Bcl2* and alpha-1,3,-mannosyl-glycoprotein 4-beta-*N*-acetylglucosaminyltransferase C (*Mgat4c*) transcripts at 24hAm and a decrease in leucyl-tRNA synthetase transcripts at 24hAm (Fig. 3*F*). The changes in these genes correlate with published data supporting the potential role of these pathways during persistent hyperammonemia in skeletal muscle (maintained cell viability (7, 8), responses to L-leucine (10)). In addition to targeted modulation of proteins, ammonia induces N-glycosylation in different proteins, but the mechanisms have not been identified (33, 34). Consistent with our data on *Mgat4c*, glycosylation levels in myotubes were increased during hyperammonemia (Fig. S5). RNA-Seq and proteomics from myotubes were then vertically integrated to determine if the proteomics data corresponded with transcriptional responses. We compared like-clusters (*e.g.*, late change RNA-Seq to late change proteomics) and dissimilar clusters (*e.g.*, early transient change RNA-Seq to late change proteomics) to help identify concordance in temporal changes in transcription and translation. Comparisons of clusters in the RNA-Seq and proteomics datasets showed that the most shared DEG/DEP were in the late change "like-clusters" (Fig. 3*G*). Of the shared DEG/DEP in late change like-clusters (n = 58), we found that the DEG and DEP expression changes were concordant in 36. We then performed Spearman correlations on the shared DEG/DEP in the late RNA-Seq–late proteomics like-clusters. Individual gene/protein correlations are shown in Fig. S6, *A* and *B*. Functional enrichment analysis demonstrated that HIF1α signaling and senescence pathways were significantly enriched in the late change clusters in both the RNA-Seq and proteomics datasets (Fig. 3*H*). Concordance and discordance between the RNA-Seq and proteomics datasets and the temporal alterations identified on cluster analyses suggests that the molecular responses occurred at the protein and mRNA levels. Whether these responses could be related to altered chromatin access was then assessed.

Hyperammonemia causes unique changes in chromatin accessibility and gene regulatory sites

To determine if changes in chromatin accessibility during hyperammonemia are consistent with the cellular RNA-Seq and proteomics patterns, the ATAC-Seq dataset from C2C12 myotubes was analyzed (Fig. 4). ATAC-Seq DAC positions and their location on the gene structure are shown in Fig. S7. Within the ATAC-Seq dataset, there were significant differences between DAC in all three treatment comparisons, with the majority (n = 1883) of DAC in the 24hAm *versus* UnT treatment comparison (Fig. 4, *A* and *B*). Functional enrichment analyses for the early transient, late, and persistent change clusters reveal enriched pathways within the ATAC-Seq dataset that are conserved across RNA-Seq and proteomics in myotubes, including pathways related to calcium, senescence, cell cycle regulation, and HIF1α signaling (Fig. 4, *C*–*E* and Fig. S8, *A* and *B*). The late change cluster on ATAC-Seq (Fig. 4*D*) showed enrichment in mRNA translation, mTOR complex, AMPK, and p65–NFκB signaling pathways that are consistent with previous experimental reports on these pathways during hyperammonemia (7, 8, 26). To determine if accessibility of regions on the same gene changes over time, early transient ATAC-Seq changes and late ATAC-Seq changes were compared for concordance between dissimilar-clusters within the same dataset. This was only possible with the ATAC-Seq dataset since the same gene can have more than one accessibility region where changes occur at different times. Since a gene can appear multiple times in ATAC-Seq data because of the presence of multiple accessibility regions, we compared the

change cluster on proteomics. *D*, heat map of myotube DEP that increase or decrease in expression significantly only at 24hAm *versus* 3hAm and/or UnT, termed late change cluster. *Stacked bar chart* showing manually curated canonical pathways that are significantly enriched in the late change proteomics cluster. *E*, heat map of myotube DEP that increase or decrease in expression significantly at 3hAm and become more/less expressed by 24hAm, termed persistent change. *Stacked bar chart* shows manually curated canonical pathways that are significantly enriched in the persistent change proteomics cluster. *F*, calcium response in differentiated myotubes to 10 mM Am compared with UnT. *G*, representative immunoblots and densitometries for validation of proteomics changes in NLR family, apoptosis inhibitory protein 1 (Naip1), myosin heavy chain (Myh), caveolin-3 (Cav-3), and B-cell lymphoma 2 (Bcl2). *H*, representative immunoblots and densitometry of cleaved caspase-3 and poly-ADP ribose polymerase-1 in UnT, 3hAm (10 mM), 24hAm (10 mM)-treated and 4-h 4 mM H_2O_2-treated differentiated C2C12 myotubes. Cell viability percentage is shown with the aforementioned treatments and also in 4-h 1 mM H_2O_2-treated cells and 4-h 8 mM H_2O_2-treated cells. *I*, representative immunoblots and densitometry of hypoxia-inducible factor 1α in myotubes. All cellular experiments were performed in three biological replicates. Significance for DEP in the cellular proteomic datasets was set at $p < 0.05$. Significance for canonical pathway enrichment was set at –log(p value) ≥1.3. *$p < 0.05$, **$p < 0.01$, and ***$p < 0.001$. All data represent mean ± SD.

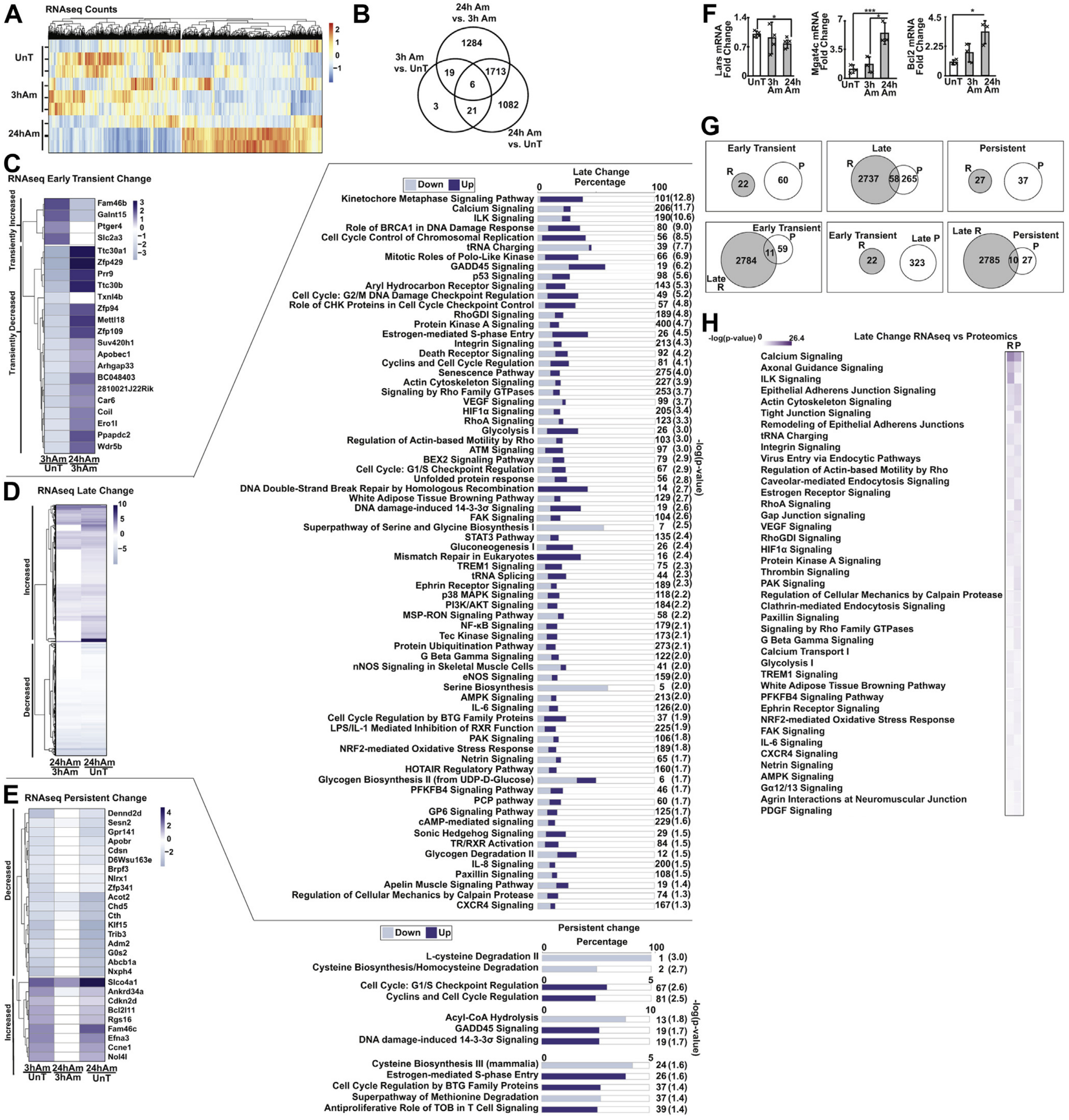

Figure 3. Differentially expressed genes in RNA-Seq from differentiated murine myotubes and as compared with myotube proteomics. *A*, heat map of differentially expressed genes (DEG) from RNA-Seq analysis of C2C12 myotubes that were either untreated (UnT) or treated for 3 h or 24 h with 10 mM ammonium acetate (Am). *B*, Venn diagram showing unique DEG in differentiated C2C12 myotubes either UnT or treated with Am and analyzed using the following comparisons: 3hAm *versus* UnT, 24hAm *versus* 3hAm, and 24hAm treatment *versus* UnT. *C*, heat map of myotube DEG that have either increased or decreased expression in 3hAm and return to baseline (UnT) status at 24hAm, termed early transient change cluster. *D*, heat map of myotube DEG that have either increased or decreased expression at 24hAm *versus* UnT/3hAm termed late change cluster. *Stacked bar chart* shows manually curated canonical pathways that are significantly enriched in the late change RNA-Seq cluster. *E*, heat map of myotube DEG that have either increased (or decreased) expression at 3hAm and whose expression increased (or decreased) further at 24hAm treatment, termed persistent change cluster. *Stacked bar chart* shows manually curated canonical pathways that are significantly enriched in the persistent change RNA-Seq cluster. *F*, real-time PCR validation of changes in select components on RNA-Seq that included leucyl-tRNA synthetase (Lars), alpha-1,3-mannosyl-glycoprotein 4-beta-*N*-acetylglucosaminyltransferase C (Mgat4c), and Bcl2 (B-cell lymphoma 2). *G*, Venn diagrams showing "like-clusters" and "dissimilar-clusters" of unique and shared genes between myotube RNA-Seq and myotube proteomics. *H*, canonical pathways enriched in late change RNA-Seq and late change proteomics clusters. All cellular experiments were performed in three biological replicates. Significance for cellular DEG was FDR <0.05. Significance for cellular differentially expressed proteins was $p <$ 0.05. Significance for canonical pathway enrichment was set at −log(p value) ≥1.3. *$p < 0.05$ and ***$p < 0.001$. All data represent mean ± SD. FDR, false discovery rate.

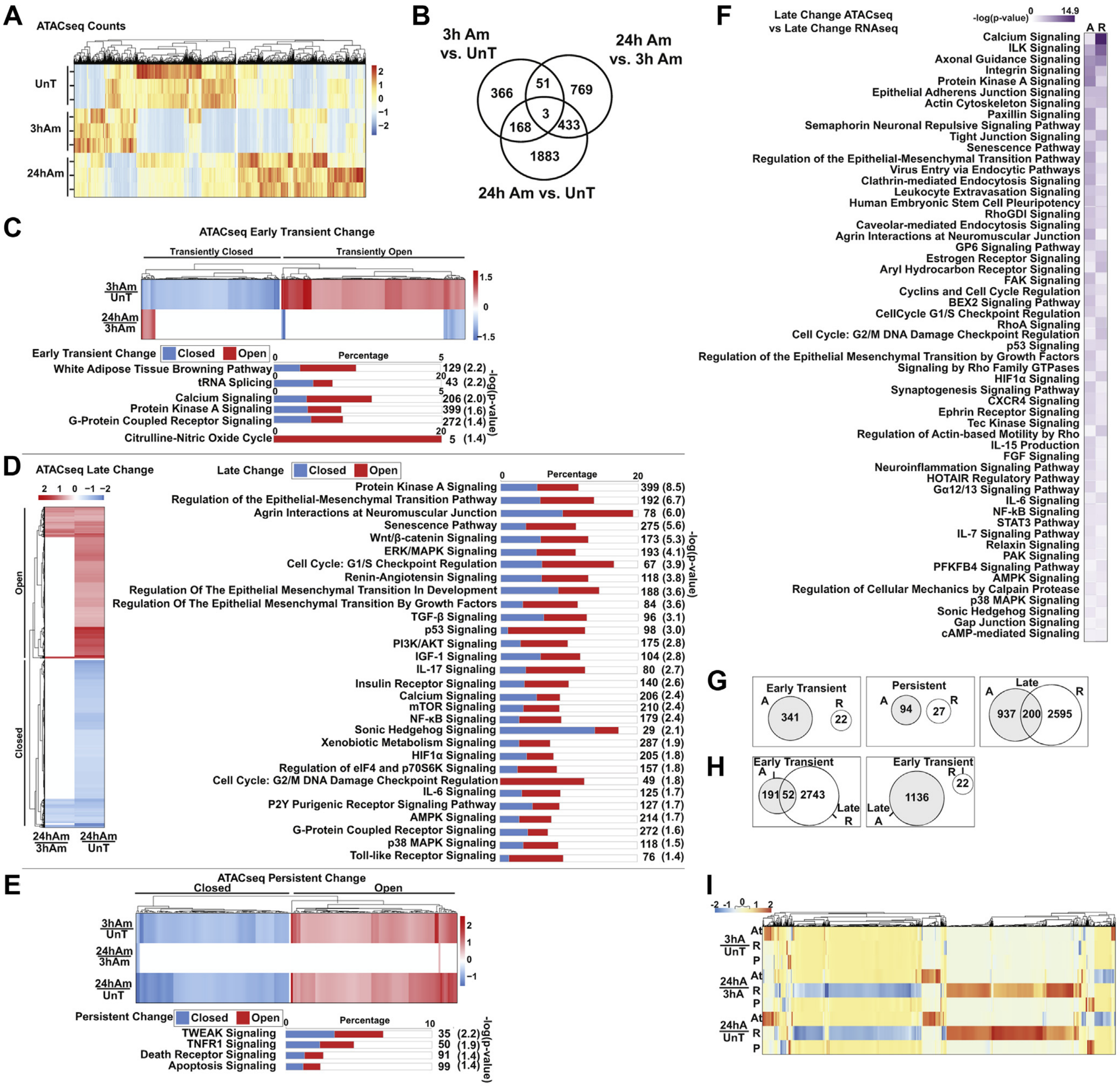

Figure 4. Unique patterns of accessible chromatin in differentiated murine myotubes during hyperammonemia are identified by ATAC-Seq. *A*, heat map of all differentially accessible chromatin (DAC) (annotated and nonannotated) from ATAC-Seq analysis of differentiated C2C12 myotubes that were either untreated (UnT) or treated with 3 h or 24 h of 10 mM ammonium acetate (Am). *B*, Venn diagram showing unique and shared DAC in UnT myotubes compared with 3hAm and 24hAm. *C*, heat map and schematic showing differential peaks that either become significantly more accessible (open) or less accessible (closed) at 3hAm returned to baseline (UnT) at 24 h, termed early transient change cluster. *Stacked bar chart* showing manually curated canonical pathways that are significantly enriched in the early transient change ATAC-Seq cluster. *D*, heat map and schematic showing differential peaks that are changed significantly only at 24hAm termed late change cluster. *Stacked bar chart* showing manually curated canonical pathways that are significantly enriched in the late change ATAC-Seq cluster. *E*, heat map and schematic showing differential peaks that open (or close) significantly at 3hAm and become more open (or more closed) at 24hAm and termed "persistent" change cluster. *Stacked bar chart* shows manually curated canonical pathways that are significantly enriched in the "persistent" change cluster. *F*, Venn diagrams of unique and shared DAC/DEG in "like-clusters," between ATAC-Seq (A) and RNA-Seq (R). *G*, Venn diagrams of unique and shared DAC/DEG in "dissimilar-clusters." *H*, integration of enriched pathways in both the late change ATAC-Seq DAC and late change RNA-Seq ordered by significance. *I*, heat map of ATAC-Seq (At), RNA-Seq (R), and proteomics (P) DAC/DEG/DEP expression levels. All cellular experiments were performed in three biological replicates. Significance for differential peaks in the ATAC-Seq dataset was set at $p < 0.005$ with fold-change cutoff $>|1.5|$. Significance for cellular DEG was set at false discovery rate (FDR) <0.05. Significance for canonical pathway enrichment was set at $-\log(p \text{ value}) \geq 1.3$. Annotation refers to a region of a known/identified gene. Nonannotated areas refer to chromosomal regions that are not in the region of known/identified genes. Like-clusters were defined as those that were temporally similar (*e.g.*, late change ATAC-Seq to late change RNA-Seq), whereas "dissimilar-clusters" were the DAC that belonged to different temporal changes in different datasets (*e.g.*, early transient change ATAC-Seq to late change RNA-Seq). ATAC-Seq, assay for transposase-accessible chromatin with high-throughput sequencing; DEG, differentially expressed gene.

trend concordance for all region combinations, and the *blue bars* in Fig. S9*A* show these ranges. A range from −1 to +1 (*e.g.*, myeloid RNA regulator of Bcl2-interacting mediator of cell-induced death [Morrbid], nuclear receptor corepressor 2) denotes that each of these genes had multiple DAC with an equal number having positive concordance (+1; same trend/agreement) and negative concordance (−1; reverse trend/discord), with the mean concordance = 0 (or undecided/indeterminate). When there are DAC on the same gene with an unequal number of concordance and discordance, the mean concordance is derived; for instance, polypeptide N-acetyl galactosaminyltransferase 2 had 1/3 agreement and 2/3 discord, therefore the overall relationship among these DAC is discordant. Based on these calculations for all 45 shared DEG/DEP/DAC, the following agreement summary was calculated: agreement = ∼49% (n = 22), discord = ∼47% (n = 21), and undecided = ∼4% (n = 2) (Fig. S9*A*). Analyses of the genes with agreement showed enrichment in cell development and differentiation (Fig. S9*B*). These data show that, similar to the patterns of responses on transcriptomics and proteomics, distinct clusters of chromosomal access alterations occurred during hyperammonemia.

Vertical integration of chromatin accessibility and transcriptomics during hyperammonemia showed most concordance in late change cluster

To determine if chromatin remodeling is linked to altered expression of genes, a vertical integration of the ATAC-Seq and RNA-Seq myotube datasets was performed. For these analyses, we only considered DAC in ATAC-Seq, which were within a known gene and thus were annotated to that gene. The greatest number of shared DAC and DEG (n = 200) were found between the late change ATAC-Seq and the late change RNA-Seq clusters (Fig. 4*F* and Fig. S9*C*). A number of DAC and DEG were shared (n = 31) between the pseudosilent clusters in both datasets (Fig. S10), supporting our interpretation that pseudosilent clusters may have biological relevance during HASR. We also noted a number (n = 52) of shared DAC and DEG in the early transient change ATAC-Seq *versus* late change RNA-Seq (Fig. 4*G*). Surprisingly, in the early transient change ATAC-Seq *versus* the late change RNA-Seq clusters, the majority (34 of 52) of shared DAC/DEG had a negative correlation (Fig. S9*D*). In the late change like-clusters between ATAC-Seq and RNA-Seq, a similar number of shared DAC/DEG showed positive and negative correlations (Fig. S9*E*), suggesting that HASR-mediated changes to chromatin most likely are not a significant driver of functional change. An alternative explanation is that even if chromatin access changes drive RNA-Seq, other upstream events and their effects can mediate these differential responses. The canonical pathways enriched in both the late change ATAC-Seq and late change RNA-Seq clusters included those previously reported to be altered during hyperammonemia (HIF1α stabilization (27); mitochondrial oxidative dysfunction (15), and others, including the senescence genes (35), consistent with our recent clinical observations supporting an accelerated aging in muscle phenotype in cirrhosis (36) (Fig. 4*H*)). An integrated heat map of ATAC-Seq, RNA-Seq, and proteomics datasets from UnT as well as 3hAm- and 24hAm-treated myotubes was generated to simultaneously represent the shared and unique changes (Fig. 4*I*) that were consistent with our analyses of each dataset (Figs. 2*B*, 3*B* and 4*B*). Other like-cluster and dissimilar-cluster comparisons and DAC/DEG/DEP accessibility/expression correlations for ATAC-Seq, RNA-Seq, and proteomics are shown in Fig. S10. Together, our combined analyses show shared genes between dataset pairs (ATAC-Seq *versus* RNA-Seq; RNA-Seq *versus* proteomics; and ATAC-Seq *versus* proteomics). However, there were very few to no shared genes across all three datasets, which may be due to differences in access, synthesis efficiency, or half-life of different molecules.

Footprinting analysis of ATAC-Seq showed enrichment of transcription factors regulating senescence and mitochondrial oxidative dysfunction during hyperammonemia

Chromosomal access regulates gene transcription by altered transcription factor binding. Footprinting analysis performed on the ATAC-Seq dataset from UnT as well as 3hAm- and 24hAm-treated myotubes (Fig. 5) identified unique and shared transcription factor motifs with significant differences between treatment time points and corresponded with predicted upstream regulators of the RNA-Seq dataset. The greatest number of unique differentially accessible motifs were found in the early transient change cluster (n = 26), whereas fewer unique motifs were identified in the late (n = 15), persistent (n = 7), and pseudosilent change (n = 10) clusters (Fig. 5, *A* and *B*). These may be due to a greater diversity of transcription factor responses that subsequently become more focused with persistent stress. Even though unique motifs from the ATAC-Seq dataset in different clusters indicated enrichment of multiple pathways (Fig. S11), the UPR and senescence pathways, including interleukin-17 signaling, were most significantly and consistently enriched in the early transient and late change clusters (Fig. 5*C*). To experimentally validate the changes in UPR pathways on footprinting analyses, we performed a UPR transcription factor activation profiling array. Interestingly, we found that the protein expression of nuclear respiratory factor-1 (NRF1), a component of the mitochondrial UPR, was upregulated with 3hAm (Fig. 5*D*). The NRF1 footprinting plot suggests an increased binding of transcription factors at the NRF1-binding site at 3hAm compared with UnT control myotubes (Fig. 5*E*). One of the functions of NRF1 is to regulate mitochondrial respiration (37, 38). Our observations of an increase in predicted binding at NRF1 motifs and on the transcription factor activation profiling array suggest that an increase in NRF1 may be a compensatory response to the mitochondrial defects during hyperammonemia that we have reported earlier (15). We then performed network analyses using the differentially accessible motifs in each cluster (Fig. S12). Based on our current analyses and published data by others and us, consistent alterations in expression of the Bcl2 and NRF1 families of genes, we generated interaction networks

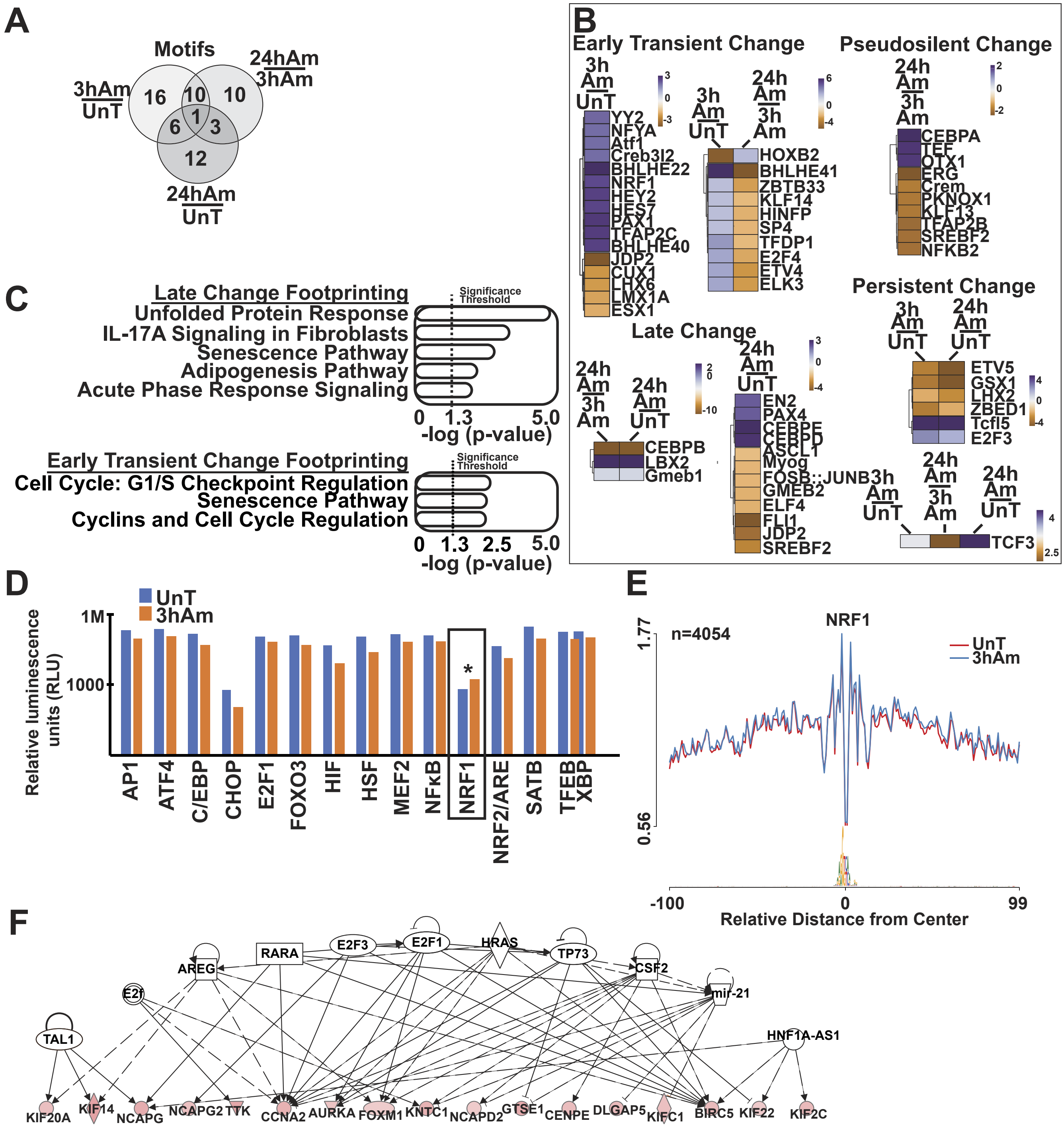

Figure 5. ATAC-Seq footprinting analysis was combined with RNA-Seq upstream regulator analysis to identify patterns of transcription factor accessibility during hyperammonemia. *A*, Venn diagram of transcription factor–binding sites (motifs) that were differentially accessible on ATAC-Seq footprinting analysis of C2C12 myotubes treated with 3 h or 24 h of 10 mM ammonium acetate (Am) compared with untreated (UnT) or 3hAm-treated myotubes. *B*, heat maps of differentially accessible transcription factor–binding sites identified on ATAC-Seq footprinting analysis of C2C12 myotubes in the early transient, pseudosilent, late, and persistent change clusters. *C*, significantly enriched canonical pathways identified in the late and early transient change clusters identified on ATAC-Seq footprinting analyses. *D*, unfolded protein response transcription factor assay for validation of ATAC-Seq footprinting analysis. *E*, ATAC-Seq footprinting plot showing decreased accessibility (indicating increased likelihood of binding) for all nuclear respiratory factor-1 (NRF1) motifs at 3hAm *versus* UnT. *F*, predicted upstream regulator network and their downstream targets in the cellular RNA-Seq differentially expressed genes (DEG) from the late change cluster. Significance for cellular RNA-Seq DEG was taken at false discovery rate (FDR) <0.05. *Red color* of genes indicates increased expression in the cellular RNA-Seq late change cluster. Significance for differentially accessible motifs was taken at $p < 0.05$. Canonical pathway enrichment significance cut off was –log(p value) ≥1.3. All cellular experiments were performed in n = 3 biological replicates. *$p < 0.05$. ATAC-Seq, assay for transposase-accessible chromatin with high-throughput sequencing.

by mapping DAC/DEG/DEP from myotubes and mouse and human muscle tissues followed by subnetworks using these two families as primary nodes (Figs. S13–S17). Previously unreported interactions between the Bcl2 family and NRF1 were identified using our vertical/horizontal integration approach. Regulation of cell cycle and senescence were major biological processes identified in these networks enriched in the footprinting analyses. Consistent with our footprinting analyses, E2F3 and E2F1, members of the E2F family of transcription factors that regulate cell cycle entry and senescence, were predicted transcriptional modulators of a significant RNA-Seq DEG network (Fig. 5*F*). Together, these findings not only help to identify hyperammonemia as a modulator of senescence but also show that our vertical integration of ATAC-Seq and RNA-Seq datasets can identify novel regulatory pathways.

Horizontal integration of proteomics across mouse muscle and myotubes showed enrichment of cell cycle regulation and ribosomal biogenesis pathways

To establish physiological relevance of our data in myotubes, we analyzed proteomics datasets *in vivo* in gastrocnemius muscle from hyperammonemic (Am mice) or control mice (n = 3 each) and integrated them with the datasets *in vitro* in myotubes (Fig. 6). A heat map (Fig. 6*A*) showed 54 DEP in gastrocnemius muscle from control or Am mice. There were multiple pathways that were enriched in the mouse muscle proteomics dataset. Of these, cell cycle regulation, HIF1α, and apoptosis signaling pathways were significantly enriched in the mouse proteomics dataset and have been previously reported to be perturbed by ammonia exposure in different cells (27, 28, 32, 35, 36) (Fig. 6*A*). We then horizontally integrated the late change cluster from myotubes and hyperammonemic mouse muscle datasets to identify shared molecules. In both the late change cluster in the cellular proteomics and in the mouse proteomics datasets, there were ten DEP that were shared, of which four were ribosomal proteins, which decreased in expression in both myotubes and mouse skeletal muscle (Fig. 6*B*) and are consistent with a reduction in ribosomal biogenesis during hyperammonemia (11). When the late change cluster from the myotube proteomics dataset was compared with the mouse proteomics dataset (Fig. 6*C*), eIF2, actin cytoskeleton, axonal guidance, actin-based motility, and other signaling pathways were enriched in both datasets. A heat map of the shared DEG/DEP between the late change cluster on RNA-Seq in myotubes and the mouse muscle proteomics dataset showed a number of skeletal muscle–specific proteins and leucyl-RNA synthetase that were altered (Fig. 6*D*). Pathway analyses using g:Profiler showed that multiple skeletal muscle contractile protein–related pathways were enriched in our mouse proteomics dataset (Fig. S18) as identified on the integrated IPA (Fig. 6*C*).

To determine if the proteomics responses in mice were related to transcriptomic changes during hyperammonemia, we analyzed the RNA-Seq from gastrocnemius muscle from control and Am mice and found 1495 DEG. A heat map analysis showed a reversal of the DEG pattern between control and Am mice (Fig. 7*A*). Functional enrichment analyses of the myotube DEG during hyperammonemia showed enrichment of calcium signaling, cell cycle regulation, death receptor, and apoptosis pathways (Fig. 7*A*). We then horizontally integrated the shared DEG as a heat map (Fig. 7*B*) followed by functional enrichment analyses of the mouse muscle and myotube late change cluster datasets (Fig. 7*C*). Calcium signaling, cell cycle signaling, oxidative stress response, and death receptor signaling pathways were enriched in both datasets (Fig. 7*C*). These pathways identified to be altered during hyperammonemia were then validated experimentally in myotubes. We show that rapid calcium flux (Fig. 2*F*), decreased apoptosis and maintained viability (Fig. 2*H*), increased expression of p21 (Fig. 7*D*), and increased mitochondrial oxidative stress, as reported by us previously (15), are components of the HASR. Concordant changes between the late change cluster on myotube RNA-Seq and hyperammonemic mouse muscle that have been previously studied in skeletal muscle were noted in actin cytoskeleton, integrin-linked kinase, and synaptogenesis signaling (Figs. 3*H*, 4*H* and 7*C* and Fig. S19). We compared the DEG/DEP from Am and control mice and noted eight shared molecules (Fig. 7*E*). A relationship between the DEG and DEP would suggest either a common regulatory mechanism between such molecules or a heretofore unknown interaction between molecules. We therefore generated a correlation matrix (Fig. 7*F*) and a pairwise correlation (Fig. 7*G*) to determine trends for proteomics and RNA-Seq expressions for the eight shared genes (number of comparisons $\binom{8}{2} = 28$). There were five positive (starch binding domain 1 [Stbd1], quinoid dihydropteridine reductase [Qdpr], COP9 signalosome subunit 5 [Cops5], AKT1 substrate 1 [Akt1s1], and adipogenesis associated Mth938 domain containing [Aamdc]) and three negative (dystrophin [Dmd], four and a half LIM domains 3 [Fhl3], and macrophage migration inhibitory factor [Mif]) correlations between the proteomics and RNA-Seq data for the eight similar DEG/DEP pairs. Consistent with these findings, when correlations were performed between pairs of dissimilar molecules, we found an inverse relation between the expression levels of two molecules in RNA-Seq and proteomics (*e.g.,* negative expression correlation between the molecule pair in RNA-Seq but positive expression correlation between the molecule pair in proteomics) when a pair of molecules contained ether DmD, Fhl3, and Mif (Fig. 7*G*). The biological and functional relevance of these novel relations needs to be evaluated in future experimental studies.

Transcriptomics from human skeletal muscle from patients with cirrhosis and hyperammonemia showed enrichment of cell cycle regulation, senescence, and mitochondrial oxidative function pathways

Finally, we asked whether changes observed in murine myotubes and skeletal muscle during hyperammonemia were also seen in human skeletal muscle tissue. A heat map of the RNA-Seq dataset from skeletal muscle from human cirrhotic (CIR) or control (CTL) subjects is shown in Figure 8. The

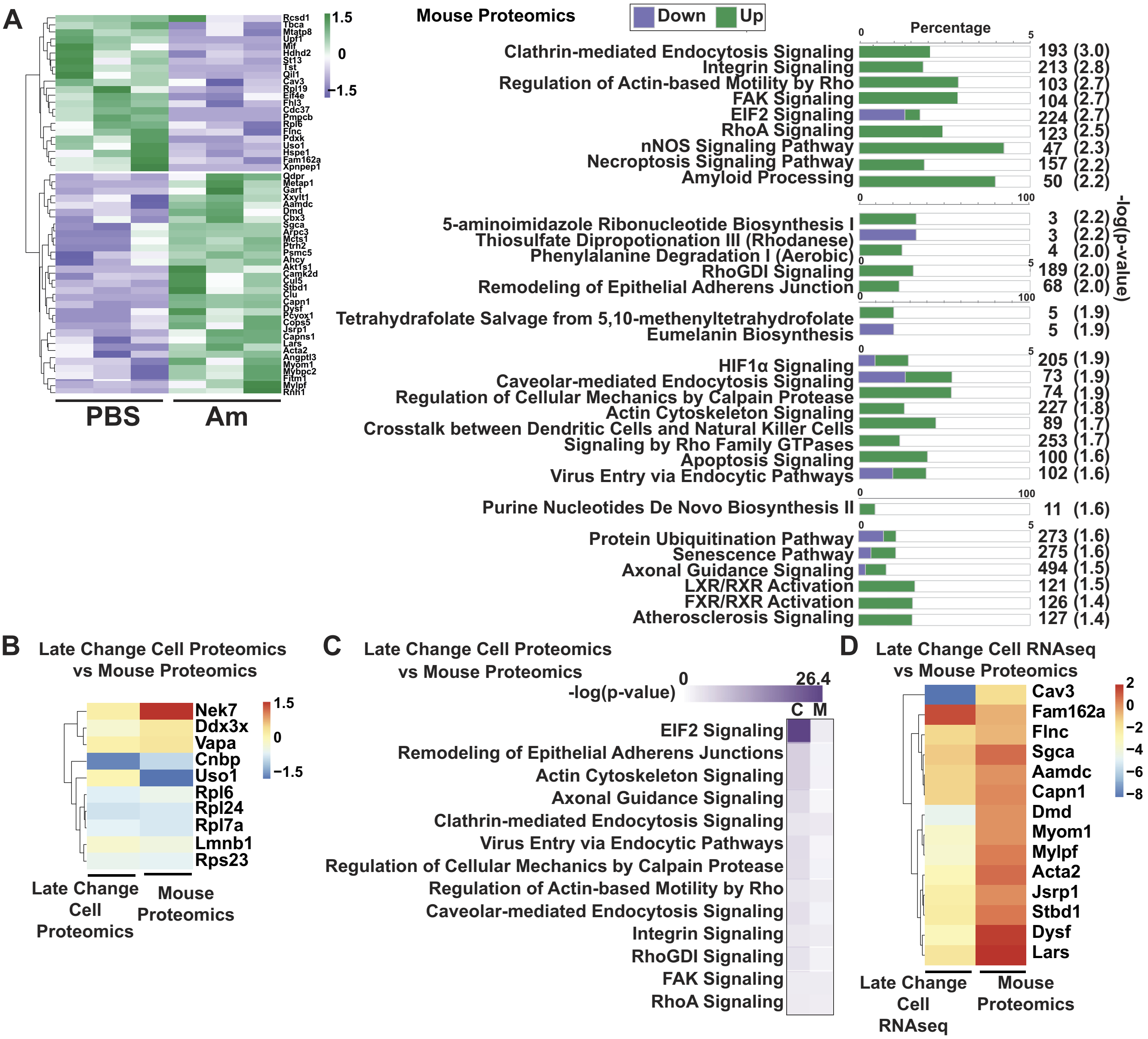

Figure 6. Mouse muscle proteomics analyses. *A*, heat map showing differentially expressed proteins (DEP) in gastrocnemius muscle from mice implanted with a miniosmotic pump releasing either ammonium acetate (Am) (2.5 $\text{mmol.kg}^{-1}.\text{d}^{-1}$) or PBS for 28 days. *Stacked bar chart* shows manually curated canonical pathways that are significantly enriched in the proteomics tissue dataset. *B*, heat map comparing the late change cluster DEP in myotubes to hyperammonemic mouse skeletal muscle DEP. *C*, integration of canonical pathways enriched in late change cluster on proteomics in myotubes and mouse muscle proteomics. *D*, heat map of shared differentially expressed genes (DEG)/DEP from the late change clusters from myotube RNA-seq and mouse muscle proteomics. All cellular experiments were performed in n = 3 biological replicates, and mouse experiments were performed in n = 3 in each group. Significance for cellular RNA-Seq DEG was taken at false discovery rate (FDR) <0.05. Significance for cellular and mouse proteomics was taken at $p < 0.05$. Canonical pathway enrichment significance cut off was –log(p value) ≥1.3. Am concentration in all cellular experiments was 10 mM.

human RNA-Seq dataset showed a reversal of expression patterns between CIR and CTL that was similar to our observations in the RNA-Seq datasets from hyperammonemic myotubes and mouse muscles (Figs. 3*A* and 7*A*). Consistent with cellular and mouse muscle transcriptomics and proteomics, cell cycle regulation, cell death, senescence, HIF1α, and oxidative stress pathways were enriched in our human RNA-Seq dataset (Figs. 8*A* and Fig. S20). Activation of the HIF1α pathway was consistent with our data in hyperammonemic myotubes (Fig. 2*D*) and mouse muscle (Fig. 6*A*) as well as previous data on HIF1α stabilization by ammonia (27, 28). TGF-β signaling pathway components were enriched in our dataset, consistent with our previous reports of increased myostatin, a member of the TGF-β superfamily, during hyperammonemia (7). Shared significant changes were also seen in Am mouse and human CIR skeletal muscle transcriptomics (n = 36), and both datasets showed enrichment of cell cycle regulation and oxidative stress response pathways (Fig. 8, *B* and *C*). Shared DEG between human and cellular transcriptomics (n = 77) showed an enrichment of cell cycle regulation, senescence, and HIF1α signaling pathways (Fig. 8, *D* and *E*). A senescence-like phenotype in a postmitotic cell

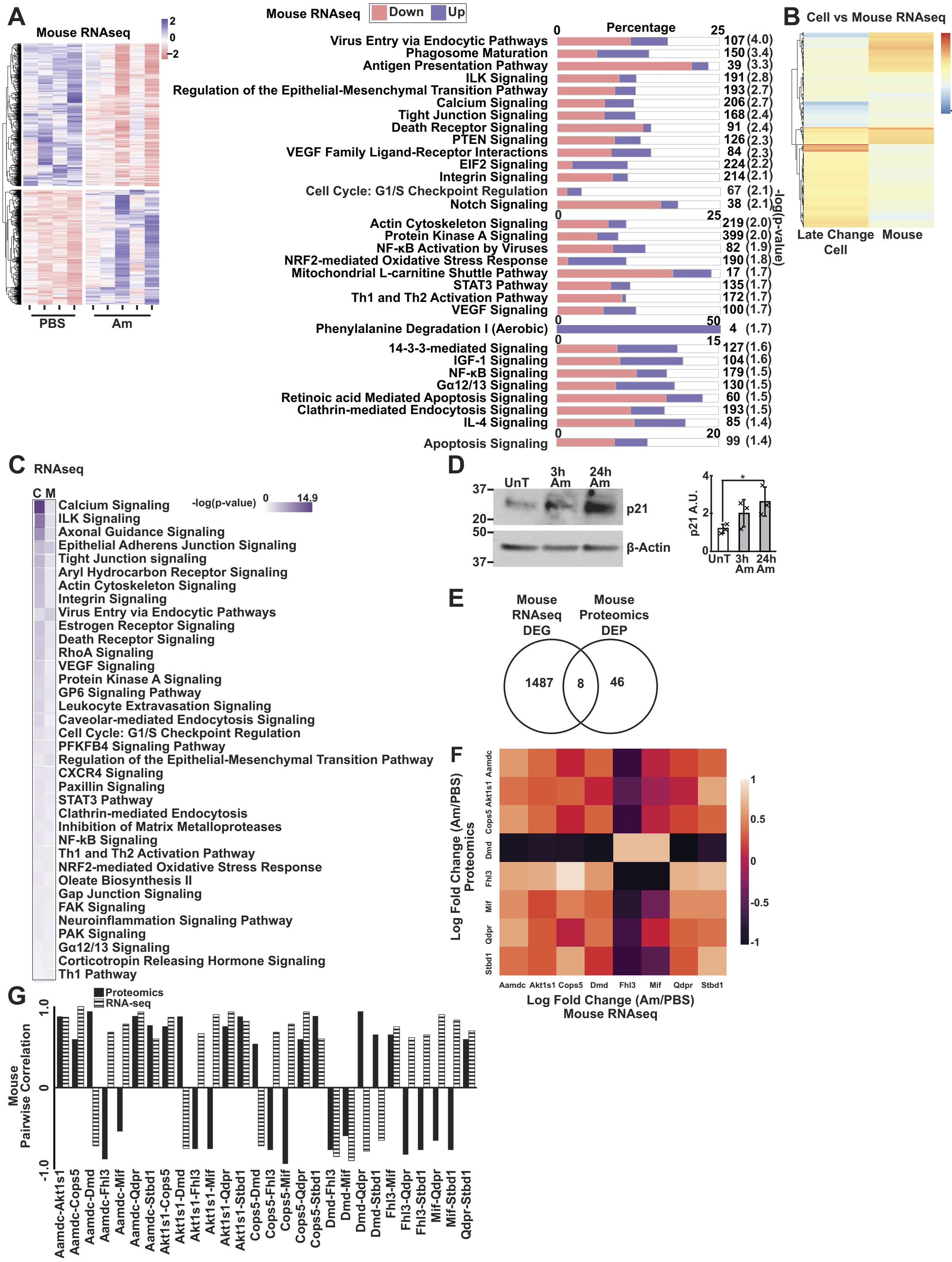

Figure 7. Mouse muscle RNA-Seq integrated with other datasets. *A*, heat map of differentially expressed genes (DEG) in the RNA-Seq dataset from gastrocnemius muscle from mice implanted with a miniosmotic pump releasing either ammonium acetate (Am) (2.5 mmol.kg^{-1}.d^{-1}) or PBS for 28 days. *Stacked bar chart* shows manually curated canonical pathways enriched in the RNA-Seq dataset from mouse muscle tissue. *B*, heat map of shared late change cluster DEG in myotubes and DEG from hyperammonemic mouse skeletal muscle. *C*, canonical pathways enriched in RNA-Seq from late change cluster in myotubes and mouse skeletal muscle. *D*, representative immunoblots and densitometry of cyclin-dependent kinase inhibitor p21 in untreated as well as 3hAm- and 24hAm-treated differentiated C2C12 myotubes. *E*, Venn diagram of unique and shared DEG between the mouse RNA-Seq dataset and the mouse proteomics dataset. *F*, correlation matrix of shared DEG/DEP expression in mouse muscle RNA-Seq and mouse muscle proteomics. *G*, pairwise correlation of shared DEG/DEP expression in mouse muscle RNA-Seq and mouse muscle proteomics. Significance for cellular RNA-Seq DEG was taken at

would typically be characterized by expression of a senescence-associated secretory phenotype. These known secretory molecules were curated from a senescence database (39) and previously published data (40) and connected in IPA. The late change cluster from the cellular RNA-Seq dataset (Fig. 8*F*) and the human RNA-Seq dataset (Fig. 8*G*) DEG expression levels were next overlaid on the senescence-associated secretory phenotype network and showed interacting nodes suggesting accelerated senescence during hyperammonemia, consistent with clinical reports of increased senescence in cirrhosis (35, 36). The DAC, DEG, and DEP from the myotube datasets and the DEG and DEP from the tissue datasets were also compared against a comprehensive senescence-associated gene database (Table S1), and we found that nicotinamide phosphoribosyltransferase, the rate-limiting enzyme in NAD biosynthesis, was increased in several datasets with hyperammonemia. Given our previous observation of decreased NAD+ during hyperammonemia, these data suggest that the increased expression of nicotinamide phosphoribosyltransferase is an adaptive response to the altered redox status (NAD+/NADH ratio). Importantly, changes in NAD+ also regulate sirtuins, critical components of cellular senescence pathway. Our approach of integrating datasets allows for identification of novel interactomes during HASR that can be targeted for therapies.

Concordance between different patterns across datasets is summarized in Table S2. The supporting data for all the figures are provided as supplementary tables indexed in Table S3. A model summarizing the major pathways enriched during early, late, and persistent hyperammonemia is shown in Fig. S21.

Discussion

Using a comprehensive approach including chromatin accessibility sequencing, transcriptomics, and proteomics, we defined the molecular landscape of hyperammonemia in myotubes and skeletal muscle. Pathways that were enriched and molecules that were upregulated/downregulated during hyperammonemia were identified and showed novel patterns of alterations that could be classified into unique clusters of responses that represent adaptive and maladaptive changes. Consistently, vertical integration of unbiased data showed temporal patterns of responses in chromatin accessibility, transcriptomics, and proteomics. Horizontal integration showed that shared responses are conserved, whereas unique responses may be related to regulatory interactions between different organs in a whole organism. These data provide novel approaches to understanding whole body and tissue-specific responses during physiological and pathological states.

There is increasing interest in integration of transcriptional and translational responses that have primarily focused on the consistency of responses (18, 23, 24, 41, 42). Discrepancies between transcripts and protein expression have been reported by others (41, 43, 44). Similarly, changes in chromatin accessibility do not always correlate with changes in gene expression. Our observations on global alterations show that a majority of gene/protein level perturbations are not concordant even though distinct clusters of responses could be identified at each level. These suggest that groups or networks of molecules interact at the chromosomal, transcriptional, and translational levels even if the exact genes/proteins within the networks do not show matching expression changes across levels. A potential reason for discordance across either the vertical (DNA, RNA, and protein) or horizontal (cell, mouse, and human) comparisons may be related to interorgan interactions/contributions to homeostatic responses; organs or tissues that alter distant organs *via* endocrine or cargo transport *via* different mechanisms, including extracellular vesicles; paracrine/extracellular matrix–mediated effects; or subcellular organelle contributions from mitochondria, endoplasmic reticulum, ribosomes, and others. Even though our studies were performed on differentiated myotubes and skeletal muscle tissue, our observations demonstrate the need to study the contributions of multiple organs/cell types when evaluating responses to perturbations in homeostasis. Studies on other organs that metabolize ammonia including the liver and brain will allow one to determine if the global responses observed in the present studies are unique to the muscle or are general responses. Our systems biology approach was reproducible across datasets and experimental models even though responses may be context dependent, and our data are limited to the skeletal muscle and myotubes.

Ideally, all measurements across the vertical regulatory program should be done simultaneously in the same cells/tissue. Since most assays for sequencing involve disrupting cellular components, simultaneous measurement of multiple molecules is not feasible. Even within a population of cells, there are differences in responses as identified by single-cell studies (45, 46). Since tissues consist of many types of cells that may respond differently to various external and internal biological processes, studies on whole tissue provides integrated data from the various groups of cells including intercellular interactions (45, 47, 48). Physiological and clinical translation of such data in tissue is further compounded by the inherent nature of regional responses in any specific organ (49, 50). Finally, heterogeneity in humans adds to the limitations and assumptions while interpreting such global regulatory responses. Understanding these methodological limitations are critical while developing a model integrating across vertical and horizontal gene regulatory phenomena. Consistently, others have reported limited correlation between mRNA and protein expression data from the same cells under similar conditions (44, 51). To reduce uncertainty, we have

---

false discovery rate (FDR) <0.05. Significance for mouse RNA-Seq was taken at $p < 0.05$, FDR <0.08. Significance for cellular and mouse proteomics was taken at $p < 0.05$. Canonical pathway enrichment significance cut off was −log(*p* value) ≥1.3. Am concentration in all cellular experiments was 10 mM. All cellular experiments were performed in n = 3 biological replicates. Mouse experiments for the RNA-Seq dataset were performed in n = 4 PBS and n = 5 Am-treated mice. *$p < 0.05$; **$p < 0.01$; and $p < 0.001$. All data represent mean ± SD.

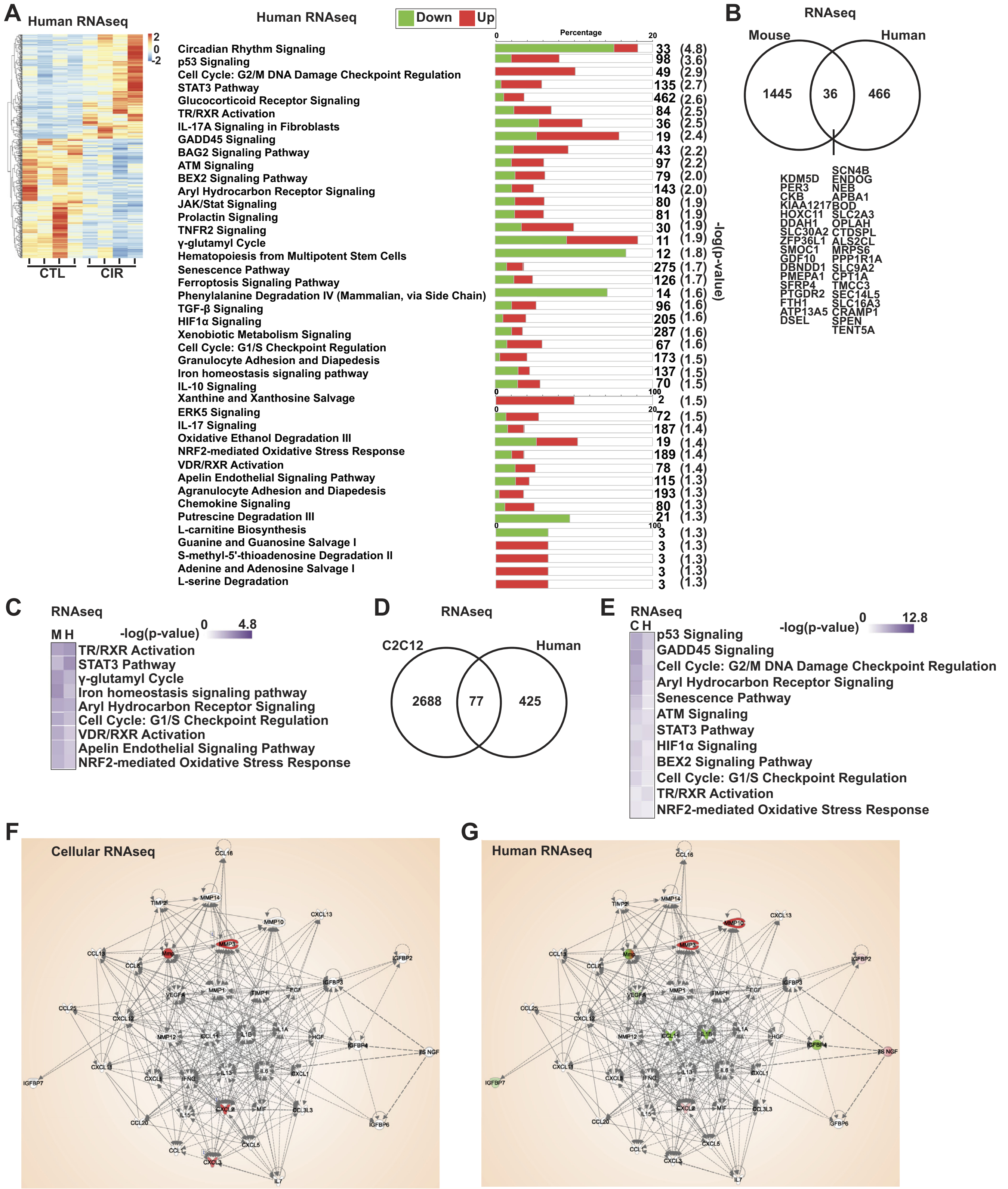

Figure 8. Human transcriptome and pathway analysis. *A*, heat map of differentially expressed genes (DEGs) and canonical pathways significantly enriched in the human skeletal muscle RNA-Seq dataset. RNA-Seq from skeletal muscle from the vastus lateralis of human patients with alcohol-associated cirrhosis (CIR) and from control patients (CTL). *B*, Venn diagram of the DEG in skeletal muscle from the hyperammonemic mouse (*versus* pair-fed) and human CIR (*versus* CTL) datasets showing unique and shared DEG. *C*, canonical pathways enriched in mouse and human muscle RNA-Seq datasets. *D*, Venn diagram of unique and shared DEG in the late change cluster in myotubes and human RNA-Seq datasets. *E*, canonical pathways enriched in the late change cluster in myotubes and human RNA-Seq datasets. *F* and *G*, senescence-associated secretory phenotype (SASP) molecules connected by known interactions and overlaid with (*F*) late change cluster cellular myotube RNA-Seq expression levels and (*G*) human RNA-Seq dataset expression levels. Significance for cellular RNA-Seq DEG was taken at false discovery rate (FDR) <0.05. Significance for mouse DEG was taken at $p < 0.05$, FDR <0.08. Significance for human DEG was

provided details of the methods used, raw data and procedures used in the analyses, and validated results of interest experimentally that allow for reproducibility of our observations. We have identified specific components for experimental validation based on previously reported data and some of the novel observations that have been suggested clinically including accelerated senescence in cirrhosis as a contributor to muscle loss (36). We anticipate that future studies will focus on evaluating other molecules/pathways noted in our large datasets.

Our data during hyperammonemia did identify a number of pathway enrichments that were conserved across datasets that were not necessarily specific for skeletal muscle responses, suggesting that many of these molecules/pathways play distinct and potentially important regulatory roles. Senescence and cell cycle regulatory pathways have been studied to a very limited extent in mature muscle cells (39, 52, 53) but were altered across datasets and in different clusters in our studies. Our data are also consistent with previous reports of ammonia-induced cellular senescence in astrocytes, which are also postmitotic cells (35). Similarly, activation of the antiapoptotic Bcl2 family members is consistent with our current observations and previous reports of unaltered cell viability despite continued HASR (9, 10). Therefore, the mechanisms that promote increased expression of Bcl2 family of proteins that protect against apoptosis in mature muscle cells during HASR need to be explored further. Our unbiased data analyses across datasets and models showed defects in mitochondrial components that were consistent with functional abnormalities reported during hyperammonemia (15). Calcium signaling is involved in a number of skeletal muscle and cellular responses, including apoptosis, mitochondrial function, and contractile responses. We observed alterations in calcium signaling during hyperammonemia across different datasets, but the mechanisms and consequences of altered calcium signaling during hyperammonemia need to be dissected in future studies. We also noted an enrichment of the HIF1α pathway during hyperammonemia that is consistent with stabilization of HIF1α. Cellular hypoxia is a possible explanation for stabilization of HIF1α during hyperammonemia. Even though we did not directly measure cellular or tissue oxygen concentrations, ammonia has not been reported to cause tissue hypoxia. A potential mechanism for stabilization of HIF1α is cataplerosis of α-ketoglutarate (15), a critical intermediary metabolite that promotes HIF1α degradation. The mechanism of HIF1α stabilization during hyperammonemia needs to be evaluated in future studies. Our novel networks and enrichment of pathways lay the foundation for discovery of novel molecules/pathways that could be therapeutic targets.

Approaches using unbiased data to comprehensively assess cellular responses at multiple levels of regulation allow for identifying novel molecules, pathways, or interactions. Each type of unbiased or “omics” data helps identify differences associated with disease or physiological changes. However, analysis of any one type of data provides correlations and does not provide insights into causal mechanisms. Therefore, because of the confounding effects of multiple potential contributors (age, sex, comorbidities, etiological agent, etc.) in complex diseases, a coordinated set of several layers of data at different time points would provide mechanistic insights into disease development. Integrations of different omics data types also provide novel insights into not only hyperammonemic responses but also help identify heretofore unrecognized pathologic effects including increased senescence. An additional consideration is the increasing use of single-cell approaches that provide the individual responses in a tissue or group of cells and allows for the identification of cells that behave differently in their interactions with other cells within a tissue. In contrast, bulk analyses of whole tissue or cell culture do not allow determination of the differential contribution of each group of cells or even individual cells to the overall responses. Single-cell analyses suffer from their own limitations, including, but not limited to, cell death of specific populations during flow cytometry, large sample input, the effects of stress related to cell separation, and the computational challenges of the bioinformatics analyses and interpretation. While horizontal integration across models can identify novel and conserved pathway enrichments, the contribution of cell–cell interactions and interorgan communication are not always accounted for, resulting in differences between models. Similarly, vertical integration can provide insights into the temporal course of responses across levels because of the time course and efficiency of transcription and translation. If there is a discord at different levels or models, a systems biology approach helps identify whether pathways are concordant or not rather than individual molecules in each pathway. Such a strategy is highly informative to determine major pathways that are responsive and how such pathways interact with each other. Discords across horizontal or vertical integrations can also impact identification of therapeutic targets. A potential approach to determining therapeutic molecules when there are differences between multiomics analyses is to experimentally validate target molecules or pathways by loss-of-function or gain-of-function studies. Such an approach was recently reported by us in two muscle model systems (54, 55). The discord on vertical and horizontal integrations observed in our studies is a potential explanation for unbiased data-based observations not consistently reproduced experimentally. Notwithstanding these limitations of multiomics analyses, our approach of vertical and horizontal integration of unbiased can identify specific contributors to global responses *in vitro* and test the physiological relevance of these observations *in vivo*. An additional advantage of our approach is the ability to determine the role of specific agents to cellular responses or disease development while providing an understanding of tissue interactions *in vivo* that modulate such responses.

---

taken at $p < 0.05$. All pathways have significance of log(p value) ≥1.3. All cellular experiments were performed in n = 3 biological replicates. Mouse experiments for the RNA-Seq dataset were performed in n = 4 PBS and n = 5 Am-treated mice. Human experiments were performed in n = 4 each for CIR and CTL. All data represent mean ± SD.

In these studies, we have defined the global responses to an endogenous cytotoxic molecule, ammonia, that may be a novel senescence-promoting molecule. Network and nodal analyses identified novel interaction partners in myotubes and skeletal muscle, and further analyses of these data can lay the foundation for studies on postmitotic cells choosing a senescence pathway to maintain viability in the face of continued stress. The present analyses also provide the basis for using integrated approaches to discover novel regulatory molecules and pathways. In summary, our data show that integrated analyses of large unbiased datasets help identify patterns of responses across chromosomes, RNA, and proteins in myotubes and skeletal muscle with experimental validation of differentially expressed molecules. The systems biology approach used in these studies will allow for novel therapeutics to be developed by combining integrated data/network analyses with bioinformatics approaches to identify treatment targets and can be applied to other model systems also.

Experimental procedures

Reagents

All chemicals were of molecular biology grade and obtained from Sigma–Aldrich. The list of reagents is shown in Table S4.

Computational resources

All computational resources used are acknowledged within the section and cited either by URL or peer-reviewed articles.

Biological resources

Human cirrhosis with hyperammonemia

Human skeletal muscle samples were obtained from the vastus lateralis in patients with alcoholic cirrhosis and healthy volunteer control subjects as previously described (56). The clinical details of these subjects have been previously reported (56). In brief, cirrhosis was diagnosed by biopsy or based on clinical presentation, laboratory values, and imaging results. A Bergström needle was used to acquire the samples that were flash frozen in liquid nitrogen and stored at −80 °C until analysis. Human studies were performed after obtaining written informed consent, and the studies were approved by the Institutional Review Board at the Cleveland Clinic and conformed to the Helsinki Declaration on human studies.

Hyperammonemic mouse

In vivo studies in ammonia-treated or vehicle-treated mice were performed in 8- to 10-week-old wildtype animals bred on a C57BL/6J background (Jackson Laboratory). In brief, an Alzet miniosmotic pump (Model 2004; Alzet) prefilled either with Am (released at a rate of 2.5 mmol/kg/day), or sterile PBS was implanted in the mice as described by us (25). Mice were sacrificed 4 weeks after pump implantation, and gastrocnemius muscle was rapidly collected and flash frozen. Plasma and muscle concentrations of ammonia were similar to those previously reported in our cellular model and human tissue (25). All animal protocols were approved by the Cleveland Clinic Institutional Animal Care and Use Committee.

Cell culture

In vitro cell culture studies were performed in differentiated murine C2C12 myotubes (American Type Culture Collection CRL 1722; American Type Culture Collection) as described by us previously (8). In brief, myoblasts were grown to 90% confluence in proliferation medium (Dulbecco's modified Eagle's medium with 10% fetal calf serum), which was replaced with differentiation medium (Dulbecco's modified Eagle's medium plus 2% horse serum) for 48 h. Cells were treated with 10 mM Am for 3 or 24 h. This model reproduces the tissue concentrations of ammonia in human skeletal muscle from patients with cirrhosis with no loss of viability (7). The cellular early and late phenotype and metabolic responses to hyperammonemia are also similar to those observed in human cirrhosis and rodent models of hyperammonemia (7–9). These concentrations of Am do not alter the cellular pH unlike that with ammonium chloride as previously reported by us (8). The molecular responses were not because of acetate as reported by us previously using 10 mM acetic acid and sodium acetate (7). Since the molecular, metabolic, and phenotypic changes with hyperammonemia develop over time, we evaluated the global responses at 3 h when we believe adaptive changes occur, based on our previously published data (11). The adaptive phase to hyperammonemia is followed by a maladaptive phase at 24 h, when HASR responses and resultant phenotypes become evident (10).

Unbiased data generated from ATAC-Seq, RNA-Seq, and proteomics were each defined as a "dataset." We generated all three datasets from myotubes, two from mouse gastrocnemius muscle (RNA-Seq and proteomics), and one (RNA-Seq) from human muscle that were used in these integrated analyses. For myotube datasets, there were three time points defined as UnT, 3hAm, or 24hAm.

ATAC-Seq

ATAC-Seq library preparation was performed using the Omni-ATAC protocol for cells (57). Sequencing and analysis were performed at the University of Michigan according to their pipeline. In brief, Snakemake was used to manage the bioinformatics workflow (58). FastQC (https://www.bioinformatics.babraham.ac.uk/projects/fastqc/) was used to assess the quality of each sample. TrimGalore (https://github.com/FelixKrueger/TrimGalore) (version 0.4.5) and Cutadapt (59) (version 1.15) were applied using the following parameters: –nextera -e 0.1 –stringency 6 –length 20 –nextseq 20. Trimmed reads were aligned to mm10 with Bowtie2 (60) (version 2.3.4.1) with the following parameters: -X 2000 –no-mixed –no-discordant, and defaults multi-seed length of 20 bp with 0 mismatches. Duplicate reads were marked with Picard (http://broadinstitute.github.io/picard/) (version 2.20.2). Alignments to autosomes were retained (while sex chromosomes and mitochondrial alignments are removed), duplicates marked by Picard were removed, and alignments below a

MAPQ threshold were removed. These filtering steps were performed with SAMtools (61) (version 1.2) and the flags: -q 10 -F 1024. Reads completely overlapping blacklisted regions (ENCODE Blacklist Regions) were removed with bedtools (62) (version 2.28.0). Sample-wise peaks were called with macs2 (63) (version 2.1.2) with flags: -f BAM –nomodel –shift -100 –extsize 200 –gsize mm. Peaks over all samples are then merged with bedops (64) (version 2.4.36). MultiQC (65) (version 1.7) generated a report combining FastQC, trimming, alignment, and duplicate calling over all the samples. For ATAC-specific QC metrics, ataqv (Ataqv) (66) was used (version 1.0.0).

Differential accessibility analysis—For each model and contrast, edgeR Bioconductor package (67) (version 3.26.8) was used to identify regions of DAC. For each sample, the number of reads in the merged peaks is counted, and a library size normalization factor is determined. The common, trended, and tagwise negative binomial dispersions of replicates are calculated. Each model is fit using the glmQLFit function, and each contrast tested with an empirical Bayes quasi-likelihood *F* test. The DAC are then annotated to genic and CpG island annotations using the annotatr Bioconductor package (68) (version 1.10.0).

Footprinting analyses—The HINT tool was used in the Regulatory Genomics Toolbox (rgt-hint) to perform footprinting and motif-binding analysis (69). Briefly, for each condition, the reads among the replicates are pooled, and tag counts are determined within the merged peaks. Motifs, or, transcription factor–binding sites, from the JASPAR database (70), were queried against the footprints found within each condition. Finally, a differential score representing the transcription factor–binding activity and the openness of the surrounding chromatin is calculated and visualized between pairs of conditions, what we refer to as “differential accessibility.”

RNA-Seq

Total RNA was extracted using the RNeasy Plus minikit (Qiagen) from C2C12 myotubes that were UnT or treated with 10 mM Am for 3 or 24 h and muscle from mice and human subjects as described by us previously (11). In brief, total RNA quality was evaluated using an Agilent 2100 bioanalyzer (Agilent Technologies) and quantitative PCR (library activity ≥2 nM), and the amount of the isolated RNA was determined using a NanoDrop ND-1000 spectrophotometer (Infinigen Biotechnology, Inc). RNA-Seq libraries were generated using the RNeasy Plus minikit (Qiagen) and sequenced on an Illumina HiSEQ400 instrument (using protocols provided by manufacturer) by Novogene (71). DEGs were identified, and their expression was compared at different times or across different datasets.

Data analysis—Downstream analysis of RNA-Seq datasets was performed using a combination of programs including STAR, HTseq, Cufflink, and Novogene’s wrapped scripts (72–74). Alignments were parsed using TopHat, and differential expressions were determined through DESeq2 (74, 75).

Reads mapping to the reference genome—*Mus musculus* genome assembly GRCm38 (mm10) and homo sapiens genome assembly GRCh37 (hg19) (https://www.ncbi.nlm.nih.gov/grc) and gene model annotation files were downloaded from genome Web site browser (National Center for Biotechnology Information [NCBI]/University of California Santa Cruz/Ensembl) directly. Reference genome indices were built using STAR, and paired-end clean reads were aligned to the reference genome using STAR (version 2.5). STAR used the method of maximal mappable prefix, which generates a precise mapping result for junction reads (72).

Quantification of gene expression level—HTSeq (73) (version 0.6.1) was used to count the read numbers mapped to each gene. The fragments per kilobase of transcript per million mapped reads value of each gene was calculated based on the length of the gene and reads count mapped to this gene. Fragments per kilobase of transcript per million mapped reads consider the effect of sequencing depth and gene length for the reads count at the same time and is currently the most commonly used method for estimating gene expression levels (76).

Differential expression analysis—Differential expression analysis between two conditions/groups (two biological replicates per condition) was performed using DESeq2 (75) (version 2_1.6.3). DESeq2 provides statistical routines for determining differential expression in digital gene expression data using a model based on the negative binomial distribution. The resulting *p* values were adjusted using the Benjamini and Hochberg’s approach for controlling the false discovery rate (FDR).

Quantitative proteomics

Global proteomics analyses were performed in myotubes and muscle tissue using methods previously described by us (11, 54). In brief, UnT and Am-treated myotube samples were prepared for unbiased proteomics studies as previously described by us (11). Murine and human tissues were flash frozen and then homogenized in a Barocycler using 30 μl lysis buffer consisting of 4 M urea in 0.1 M ammonium bicarbonate with fresh Complete Mini Protease Inhibitor Cocktail (Roche) added. The homogenizing temperature was set at 35 °C, 90 cycles with 20 s at 45 PSI, and 10 s at 0 PSI per cycle. After homogenization, the tissue was centrifuged and the supernatant was transferred to a new Eppendorf tube. Proteins were digested with trypsin and prepared for MS; unbiased proteomics studies were performed on a Thermo Scientific Fusion Lumos MS system (Thermo Scientific), and data were analyzed using MaxQuant software (version 1.6.3.3) as previously described by us (11) to identify DEP.

Digested peptides were analyzed on a ThermoFisher Scientific UltiMate 3000 UHPLC system (ThermoFisher Scientific) interfaced with a ThermoFisher Scientific Orbitrap Fusion Lumos Tribrid mass spectrometer (Thermo Scientific). Liquid chromatography was performed prior to MS/MS analysis for peptide separation. The HPLC column used is a Thermo Scientific Acclaim PepMap 100 C18 reversed-phase capillary chromatography column (Thermo Fisher Scientific) 75 μm × 15 cm, 2 μm, 100 Å. About 5 μl volumes of the peptide extract were injected, and peptides were eluted from the column by a 110-min acetonitrile/0.1% formic acid gradient at a flow rate of 0.30 μl/min and introduced to the source of the mass spectrometer online. Nano electrospray ion source was operated at 2.5 kV. The digest was analyzed using the data-dependent multitask capability of the instrument acquiring full scan mass spectra using an FT orbitrap analyzer to determine peptide molecular weights and collision-induced dissociation MS/MS product ion spectra with an ion-trap analyzer at 35% normalized collision energy to determine the amino acid sequence in successive instrument scans. The MS method used in this study was a data-dependent acquisition with 3 s duty cycle. It includes one full scan at a resolution of 120,000 followed by as many MS/MS scans as possible on the most abundant ions in that full scan. Dynamic exclusion was enabled with a repeat count of 1, and ions within 10 ppm of the fragmented mass were excluded for 60 s.

The LC–MS-based quantitative proteomic experiments were done using three biological replicates in each treatment group with one technical replicate per sample. The proteins with single-peptide identifications were removed. The data were analyzed using MaxQuant, version 1.6.3.3 with the search engine Andromeda, which is integrated in MaxQuant software, and the parameters used were default settings for an Orbitrap instrument. The database used to search the MS/MS spectra was the UniprotKB/Swiss-Prot with organism set to mouse containing 25,035 entries downloaded on July 26, 2017 with an automatically generated decoy database (reversed sequences). The search was performed looking for fully tryptic peptides with a maximum of two missed cleavages. Oxidation of methionine and acetylation of protein N terminus were set as dynamic modifications, and carbamidomethylation of cysteine was set as static modifications. The precursor mass tolerance for these searches was set to 20 ppm, and the fragment ion mass tolerance was set to 0.5 Da. The search was performed including the common contaminant database available in MaxQuant, and these proteins were excluded in the data analysis. An FDR was set to 1% for both peptide and protein identification and calculated using the number of identified peptides/proteins from decoy database divided by the total number of identified peptides/proteins. Two peptides were required for positive protein identification to decrease the chance of false discovery by a random match. The "match between runs" feature of MaxQuant was used to transfer identifications to other LC–MS/MS runs based on their masses and retention time (maximum deviation of 0.7 min), and this was also used in quantification experiments. Quantifications were performed using the precursor intensity–based label-free quantitation method available in the MaxQuant program (77). The resulting label-free quantification intensities were used as the measures of protein quantities in this work and include accession number (and database from which it is derived), the number of distinct peptides assigned for each protein, percentage coverage of each protein assigned, and the quantification measurements for each protein (Tables S5 and S6).

Vertical integration

Comparing responses across different unbiased datasets (ATAC-Seq, RNA-Seq, and proteomics) from the same sample source were defined as "vertical integration" because it allows us to determine the consistency of expression across these datasets. Vertical integration was performed by comparing *in vitro* results in myotubes. Vertical integration of *in vivo* RNA-Seq and proteomics was performed for murine skeletal muscle.

Horizontal integration

Comparison of unbiased datasets from different sample sources (*e.g.*, RNA-Seq from myotubes, muscle tissue from mice and human subjects) was defined as horizontal integration because it allows us to determine the degree of conserved responses across species/sources. Unbiased *in vitro* data from myotubes and unbiased *in vivo* data from gastrocnemius muscle from hyperammonemic and pair-fed mice and human skeletal muscle from cirrhotic patients and controls were then compared to determine unique and shared characteristics of datasets across tissue and species.

Hierarchical clustering and heat map generation

Sample heat maps were created using "pheatmap" (https://cran.r-project.org/web/packages/pheatmap/index.html), and rows were scaled. Hierarchical clustering was performed using hclust (https://www.rdocumentation.org/packages/fastcluster/versions/1.1.25/topics/hclust) using complete-linkage clustering, and dendrograms were plotted with dendextend (78).

Cluster analyses

DAC/DEG/DEP studied in the datasets from the three time points—UnT, 3hAm-treated, and 24hAm-treated myotubes, showed distinct patterns or clusters (Fig. S1). Significant changes (increase or decrease in expression) at 3hAm compared with UnT but not with 24hAm *versus* UnT was called an "early transient" change. We termed a significant difference in accessibility/expression between 24hAm *versus* 3hAm, but without a difference in either 3h or 24hAm from UnT, as "pseudosilent." We used this term because accessibility/expression changes from baseline are not significant at 3h or 24h and in classical analyses comparing responses with baseline control would have been identified to have no significant difference. A "late" change was defined as significant change in accessibility/expression between UnT and 24hAm but not at 3hAm *versus* UnT. "Persistent" change was defined as a change in the same direction (increase or decrease in accessibility/expression) at 3hAm and 24hAm compared with UnT. Cluster patterns were then compared during vertical integration to determine if there was a pattern or temporal course of accessibility/expression to evaluate if chromosomal access results in translation and if mRNA expression correlates with protein expression. Since the temporal course of transcription and translation depends on a number of factors, we used "like-cluster" and "dissimilar-cluster" integration. Like-clusters were defined as those that were temporally similar, (*e.g.*, late change ATAC-Seq to late change RNA-Seq), whereas "dissimilar-clusters" were the differentially accessible/expressed chromatin/mRNA/proteins that belonged to different temporal changes in different datasets (*e.g.*, early transient change ATAC-Seq to late change RNA-Seq). A dissimilar-cluster relation would suggest that in addition to the time/efficiency of transcription/translation, stability of the molecules also affects the observed responses.

Correlation analyses

ATAC-Seq, RNA-Seq, and proteomics myotube and skeletal muscle tissue datasets, as well as the four temporal cluster patterns, early transient, pseudosilent, late, and persistent change, were analyzed. We performed intersections for the "like-clusters" for the different datasets to retrieve the shared gene list between a dataset pair for a cluster type. Dataset pairs of shared DAC/DEG/DEP were then generated by paired vertical analyses, for example, ATAC-Seq–RNA-Seq; RNA-Seq–proteomics; and ATAC-Seq–proteomics. Genes shared between datasets for each of the four "like-clusters" were also identified. Correlations between dataset pairs for accessibility/expression values in a certain change category were performed. Since the early transient and persistent clusters did not have any shared genes, we only performed the correlation analysis for late and pseudosilent clusters. In this analysis, we examined whether concordance between expression/accessibility trends at various characterization levels is temporally determined and if the changes that occurred in chromosomal accessibility, for example, are followed by changes at another level (*e.g.*, transcription) instantaneously or with some time delay.

For each dataset pair, we calculated the correlations using two approaches:

(a) *Correlation for DAC/DEG/DEP*. We consider the treatment comparisons (*e.g.*, 24hAm *versus* 3hAm in one of the dataset clusters) as samples and the shared DAC/DEG/DEP as variables to calculate the correlation between accessibility/expression changes for a dataset pair. This will generate values of +1 or −1 only (*i.e.*, trend), since only two treatment comparisons are available at most per gene. We then summarized the overall trend agreements by using the sign of the mean correlation where positive corresponds to agreement, negative to discord, and a zero value is interpreted as undecided. This correlation analysis could not be performed for the pseudosilent category as only one treatment comparison (24hAm *versus* 3hAm) was available for comparison between datasets.

(b) *Correlation for clusters*. We consider the DAC/DEG/DEP as samples and the clusters as variables to calculate the correlation between accessibility/expression changes for a dataset pair. This generated values in the usual [−1, 1] range since multiple samples can be available per variable. This yielded low-to-moderate correlations ($|r| < 0.5$) for both late and pseudosilent clusters.

Next, we sought to perform analogous correlation analyses between datasets and clusters and retrieved the shared DAC/DEG/DEP in a similar fashion. This yielded 36 distinct sets of shared DAC/DEG/DAP (6 × 6, number of change category pairs $\binom{4}{2} = 6$, and number of dataset arrangements = ${}^{3}_{2}P$). We can only determine the correlation between dataset clusters for DAC/DEG/DAP if the number of treatment comparison groups within a cluster is the same, which is true for the early–late change dissimilar-clusters only. We then get the trend agreement summary, which has a 35 to 65% split between "agreement" and "discord." Contrarily, we can calculate the correlations for shared treatment comparison groups for any dissimilar-cluster given that we have nonzero accessibility/expression values for the shared DAC/DEG/DAP. We calculate these correlations for early–late, early–pseudosilent, late–persistent, and late–pseudosilent clusters, which show variation in both correlation trends and values, that is, $-1 < r < 0.5$. We cannot calculate the correlations for the early–persistent and persistent–pseudosilent dissimilar-clusters as they either do not have enough shared DAC/DEG/DAP or only have an expression value of zero.

Also, we can find shared DAC for dissimilar-clusters within the ATAC-Seq dataset because of the possibility of having multiple different DAC sites within the same gene displaying different directional trends in different clusters. We calculate the temporal change correlations for all three treatment comparisons between six ATAC-Seq dataset pairs from the three change categories, which show a shared trend with wide range, that is, $0.1 < r < 0.8$.

Functional enrichment analyses

A number of gene interaction analytical tools were used to evaluate known or reported interactions and expected responses using our experimental data. The most frequently used applications include IPA (QIAGEN, Inc; https://www.qiagenbioinformatics.com/products/ingenuity-pathway-analysis) that uses proprietary algorithms and knowledge database and g:Profiler (https://biit.cs.ut.ee/gprofiler/gost), which includes analyses from Kyoto Encyclopedia of Genes and Genomes (https://www.kegg.jp) that uses molecular-level information generated by genome sequencing and other high-throughput experimental strategies, and GO (http://geneontology.org) that was developed by a consortium (GO consortium) that developed a comprehensive computational model of biological systems, and the TRANSFAC database of transcription factors (79), among others. Even though these tools use experimental published data, the priorities provided and the weights for the algorithms are different and hence analyzing the same experimental data can provide different results in terms of networks and regulatory molecular pathways. Therefore, we used both IPA and the databases accessible in g:Profiler to determine common and unique pathways/networks identified from our large datasets.

IPA

ATAC-Seq DAC and motif accessibility data (footprinting analyses), RNA-Seq DEG, and proteomics DEP expression and statistical significance values were uploaded to IPA

(QIAGEN, Inc; https://www.qiagenbioinformatics.com/products/ingenuity-pathway-analysis) and canonical pathway enrichment, or the pathways with the most significant representation among the molecules in the selected dataset, were identified using the Ingenuity Pathway Knowledge Base (IPKB).

Networks of upstream regulators and networks of molecules with known interactions were also generated using the IPKB. All the molecules that compose each network identified in the IPKB are listed, and the molecules from the gene set that are contained within a network, termed "network eligible molecules," are quantified. Regulatory networks of these unique and shared genes for temporal clusters and datasets were generated and integrated for qualitative comparisons. The upstream regulator analysis tool was used to analyze linkages to RNA-Seq DEGs *via* coordinated expression levels found within a dataset in order to identify potential upstream regulators of the RNA transcription.

g:Profiler

Lists of differentially accessible/expressed genes were inputted into g:Profiler (80) (version e102_eg49_p15_7a9b4d6), freely available at https://biit.cs.ut.ee/gprofiler/gost. Using the g:Ost tool, multiple databases of functional evidence including GO terms, biological pathways, regulatory motifs of transcription factors and microRNAs, human disease annotations, and protein–protein interactions were mined for the functional enrichment analyses performed.

Senescence database analyses

The Cell Senescence Gene Database was used to identify known senescence genes (39) in our ATAC-Seq, RNA-Seq, and proteomics data.

Validation of representative observations

To confirm the validity of our unbiased data observations and analyses, mRNA was quantified by real-time PCR using methods previously described (8). In brief, total RNA was extracted from myotubes, reverse transcribed to complementary DNA, and amplified on an Applied Biosystems7500 real-time PCR instrument (Thermo Fisher Scientific), and the PCR product was run on a Tris borate EDTA gel with ethidium bromide staining. The primer sequences were leucine t-RNA synthetase (F5′-cgacccctgacgtgctataa-3′; R5′-ctgcaagatcatccggggaa-3′); Mgat4c (F5′-acagtgttctttgcaagagccgc-3′; R5′-tgggaacgtgcttcatggaccaa-3′), and Bcl2 (F5′-acctgcagcttcttttcggggaa-3′; and R5′-attgggttgctctcaggctggaa-3′). Results were normalized to β-actin (F5′-atcgtgcgtgacatcaaga-3′; R5′-atgccacaggattccata-3′). Immunoblots were performed in proteins extracted from myotube lysate, quantified, and subjected to gel electrophoresis, electrotransferred to polyvinylidene fluoride membrane, and blotted for NLR family apoptosis inhibitory protein-1 (R&D Systems), caveolin-3 (Novus), myosin heavy chain (Millipore), p21 (Proteintech), cleaved caspase-3 and PARP/PARP1 (Cell Signaling Technologies), Bcl-2 (BioVision), O-linked *N*-acetylglucosamine (AbCam), and HIF1-α (Cell Signaling Technologies) primary antibodies at 1:1000 dilution and appropriate secondary antibodies (1:10,000), and developed using enhanced chemiluminescence solution (Thermo Fisher Scientific). Densitometries were performed using ImageJ (National Institutes of Health) (81).

An activation profiling array to determine 16 UPR-related transcription factors simultaneously was used using the manufacturer protocol (Signosis, Inc). We determined the activation of these transcription factors in differentiated myotubes at 3hAm. Nuclear protein extracts were prepared using the Nuclear Extraction Kit protocol (SK-0001; Signosis, Inc). In brief, a series of biotinylated probes made from consensus sequences of transcription factor DNA-binding sites were incubated with nuclear extracts, and the transcription factor–probe complex was separated from free probes using a spin column. The bound probes were separated from the complex and hybridized with complementary sequences of the probes on a plate and detected using a streptavidin-horseradish peroxidase conjugate. Luminescence was determined on a microplate luminometer.

Cell death

Apoptosis was determined using annexin V tagged to Alexa Fluor 680 by flow cytometry as described by us earlier (54). In brief, differentiated C2C12 myotubes that were treated with 10 mM Am or equal volume of medium for 3 h and 24 h and 1 mM hydrogen peroxide for 4 h at 37 °C prior to trypsinization and flow cytometry analysis (LSRII from BD Biosciences). Analysis was done using the FlowJo software (FlowJo, LLC). Cell viability was quantified by trypan blue exclusion as described by us previously (54).

Calcium concentrations

Cellular calcium levels were measured using FLIPR Calcium 5 Assay Kit (Molecular Devices) as described previously (82). Differentiated myotubes were seeded at a density of 100,000 cells/well in a 96-well clear bottom black plate. Following serum starvation, calcium-sensitive dye was added to the cells. The Flipper instrument was programmed in FLEX mode to add ligands (0.04 and 1000 nM concentration) to the cells and to monitor the fluorescence before and after adding 10 mM Am. The response curves were plotted and expressed as relative fluorescence units.

Statistical approach

In order to have a range of 50 to 2800 DAC/DEG/DEP from each cluster or dataset for functional enrichment analysis, we slightly varied the significance and fold-change cutoffs for DAC, DEG, and DEP, respectively. Given the multiple analyses and models of *in vitro* and *in vivo* hyperammonemia, this was the tightest range we could achieve while keeping the significance cutoffs similar to other published data, the same within each dataset, and within a myotube dataset, the same for each cluster. Because footprinting analysis was a subanalysis within the ATAC-Seq dataset, we did not choose the significance level to stay within the goal range of 50 to 2800 differentially accessible motifs per cluster but instead used the least conservative significance cutoff applied to any other dataset within this study, $p < 0.05$.

The following specific significance cutoffs were utilized: ATAC-Seq DAC $p < 0.005$ and a fold-change cutoff of $>|1.5|$; ATAC footprinting motif differential activity $p < 0.05$; cellular RNA-Seq DEG FDR <0.05; tissue RNA-Seq DEG $p < 0.05$ FDR <0.08; cellular and tissue proteomics DEP $p < 0.05$. Canonical pathways were determined to be significant if $-\log(p$ value) ≥ 1.3 for the pathway. Validation data are presented as mean ± SD and an unpaired Student's t test was used to assess statistical significance. The biological replicates used for each dataset were as follows: n = 3 per treatment group for all cellular datasets and mouse skeletal muscle proteomics; n = 4 for PBS and n = 5 for Am-treated mouse skeletal muscle RNA-Seq; n = 4 for each group for human skeletal muscle RNA-Seq. For the canonical pathway enrichment of IPAs, the significance values (p value of overlap with a dataset) are calculated using a right-tailed Fisher's exact test. The significance indicates whether the percentage of DAC/DEG/DEP associated with a pathway is present in our datasets/clusters by random chance. For the IPA network analyses, a significance score is given to each network by taking the negative exponent of the right-tailed Fisher's exact test result. The score measures the likelihood that the "network eligible" molecules that are part of a network are found within the dataset by random chance alone (83). For g:Profiler functional enrichment analyses, the g:SCS multiple testing correction method was used, applying a significance threshold of 0.05 (80).

Reliability of the measurements between replicates

The raw values for the biological replicates for unbiased data were used for generating heat maps and all raw values (including those differentially expressed between datasets) been provided as Supporting Tables. For pathway analyses, fold changes were calculated for each differentially expressed molecule (DAC, DEG, and DEP) by averaging the control and hyperammonemic groups. For unbiased data analyses, false discovery rates, raw data, $\log_2$ fold change, and p values are provided for all data.

Data availability

The unbiased data in this article are available in the Supporting Tables and also publicly available at established repositories as follows. The cellular RNA-Seq datasets are publicly available at NCBI Sequence Read Archives database accession: PRJNA495054 and have been previously published (11). The other high-throughput sequencing data (the cellular ATAC-Seq dataset and human and mouse RNA-Seq datasets) from this study are available at NCBI Gene Expression Omnibus as a superseries with accession number GSE171645 and can be directly located at the following URLs:

https://www.ncbi.nlm.nih.gov/geo/query/acc.cgi?acc=GSE171642

https://www.ncbi.nlm.nih.gov/geo/query/acc.cgi?acc=GSE171643

https://www.ncbi.nlm.nih.gov/geo/query/acc.cgi?acc=GSE171644

The MS proteomics data have been deposited to the ProteomeXchange Consortium *via* the PRIDE (84) partner repository (http://www.proteomexchange.org) with dataset identifier PXD026955 and 10.6019/PXD026955. The flow cytometry data are available at FlowRepository (https://flowrepository.org) under repository ID: FR-FCM-Z3MS. No new software code was written for this article. All other data are contained within the article.

Supporting information—This article contains supporting information.

Author contributions—N. W. and S. D. conceptualization; N. W., S. S. S., A. K., S. S. K., and S. D. methodology; N. W. and S. D. software; N. W., S. S. S., A. K., S. S. K., and S. D. validation; N. W., S. S. S., A. K., S. R. D., S. M., J. S., A. B., A. H. A., A. C., B. B. W., L. L., Z. H., K. E., M. S. L., Y. M. S., G. D., R. P., and S. D. formal analysis; N. W., S. S. S., A. K., S. S. K., and S. D. investigation; N. W. and S. D. resources; N. W., S. S. S., A. K., S. R. D., S. M., J. S., A. B., A. H. A., A. C., B. B. W., L. L., M. S. L., Y. M. S., G. D., R. P., and S. D. data curation; N. W., A. K., and S. D. writing–original draft; N. W., S. S. S., A. K., S. R. D., S. M., J. S., A. B., A. H. A., A. C., B. B. W., L. L., Z. H., S. S. K., K. E., M. S. L., Y. M. S., G. D., R. P., and S. D. writing–review and editing; N. W., A. K., and S. D. visualization; N. W., S. S. K, and S. D. supervision; N. W. and S. D. project administration; N. W. and S. D. funding acquisition.

Funding and additional information—S. D. is partially supported by the National Institutes of Health (NIH) RO1 GM119174; RO1 DK113196; P50 AA024333; RO1 AA021890; 3U01AA026976-03S1; UO1 AA 026976; R56HL141744;UO1 DK061732; 5U01 DK062470-17S2; R21 AR 071046 (also G. D. is supported); and the Howard and Helen Trevey Endowment. N. W. is partially supported by the NIH K08 AA028794 and the American College of Gastroenterology Clinical Research Award. The proteomics core is partially supported by the NIH shared instrument grant 1S10OD023436-01. A. H. A. and N. W. were supported by K12 HL141952. M. S. L. was supported by the NIH R21AI153780, Velosano grant, Department of Defense grant no. PR150084, and by Cure for IBD. Y. S. S. was supported by R01CA148828, R01DK095201, and R01CA245546. The content is solely the responsibility of the authors and does not necessarily represent the official views of the NIH.

Conflict of interest—The funders had no role in the design, performance, or interpretation of these studies. The authors declare that they have no conflicts of interest with the contents of this article.

Abbreviations—The abbreviations used are: Am, ammonium acetate; AMPK, AMP-activated protein kinase; ATAC-Seq, assay for transposase-accessible chromatin with high-throughput sequencing; Bcl2, B-cell leukemia/lymphoma 2; CIR, cirrhotic; CTL, control; DAC, differentially accessible chromatin; DEG, differentially expressed genes; DEP, differentially expressed proteins; eIF2α, eukaryotic initiation factor-2α; FDR, false discovery rate; GO, Gene Ontology; HASR, hyperammonemic stress response;

HIF1α, hypoxia-inducible factor 1-alpha; IPA, ingenuity pathway analysis; IPKB, Ingenuity Pathway Knowledge Base; Mgat4c, alpha-1,3,-mannosyl-glycoprotein 4-beta-*N*-acetylglucosaminyltransferase C; mTOR, mammalian target of rapamycin; NCBI, National Center for Biotechnology Information; NIH, National Institutes of Health; NRF1, nuclear respiratory factor-1; PARP1, poly(ADP-ribose) polymerase 1; TGF-β, transforming growth factor β; UnT, untreated; UPR, unfolded protein response.

References

1. Adeva, M. M., Souto, G., Blanco, N., and Donapetry, C. (2012) Ammonium metabolism in humans. *Metabolism* **61**, 1495–1511
2. Walker, V. (2014) Ammonia metabolism and hyperammonemic disorders. *Adv. Clin. Chem.* **67**, 73–150
3. Dasarathy, S., Mookerjee, R. P., Rackayova, V., Rangroo Thrane, V., Vairappan, B., Ott, P., and Rose, C. F. (2017) Ammonia toxicity: From head to toe? *Metab. Brain Dis.* **32**, 529–538
4. Dasarathy, S., and Hatzoglou, M. (2018) Hyperammonemia and proteostasis in cirrhosis. *Curr. Opin. Clin. Nutr. Metab. Care* **21**, 30–36
5. Lockwood, A. H., McDonald, J. M., Reiman, R. E., Gelbard, A. S., Laughlin, J. S., Duffy, T. E., and Plum, F. (1979) The dynamics of ammonia metabolism in man. Effects of liver disease and hyperammonemia. *J. Clin. Invest.* **63**, 449–460
6. Ganda, O. P., and Ruderman, N. B. (1976) Muscle nitrogen metabolism in chronic hepatic insufficiency. *Metabolism* **25**, 427–435
7. Qiu, J., Thapaliya, S., Runkana, A., Yang, Y., Tsien, C., Mohan, M. L., Narayanan, A., Eghtesad, B., Mozdziak, P. E., McDonald, C., Stark, G. R., Welle, S., Naga Prasad, S. V., and Dasarathy, S. (2013) Hyperammonemia in cirrhosis induces transcriptional regulation of myostatin by an NF-kappaB-mediated mechanism. *Proc. Natl. Acad. Sci. U. S. A.* **110**, 18162–18167
8. Qiu, J., Tsien, C., Thapalaya, S., Narayanan, A., Weihl, C. C., Ching, J. K., Eghtesad, B., Singh, K., Fu, X., Dubyak, G., McDonald, C., Almasan, A., Hazen, S. L., Naga Prasad, S. V., and Dasarathy, S. (2012) Hyperammonemia-mediated autophagy in skeletal muscle contributes to sarcopenia of cirrhosis. *Am. J. Physiol. Endocrinol. Metab.* **303**, E983–E993
9. Kumar, A., Davuluri, G., Silva, R. N. E., Engelen, M., Ten Have, G. A. M., Prayson, R., Deutz, N. E. P., and Dasarathy, S. (2017) Ammonia lowering reverses sarcopenia of cirrhosis by restoring skeletal muscle proteostasis. *Hepatology* **65**, 2045–2058
10. Davuluri, G., Krokowski, D., Guan, B. J., Kumar, A., Thapaliya, S., Singh, D., Hatzoglou, M., and Dasarathy, S. (2016) Metabolic adaptation of skeletal muscle to hyperammonemia drives the beneficial effects of L-leucine in cirrhosis. *J. Hepatol.* **65**, 929–937
11. Davuluri, G., Giusto, M., Chandel, R., Welch, N., Alsabbagh, K., Kant, S., Kumar, A., Kim, A., Gangadhariah, M., Ghosh, P. K., Tran, U., Krajcik, D. M., Vasu, K., DiDonato, A. J., DiDonato, J. A., *et al.* (2019) Impaired ribosomal biogenesis by noncanonical degradation of beta-catenin during hyperammonemia. *Mol. Cell. Biol.* **39**, e00451-18
12. Olde Damink, S. W., Deutz, N. E., Dejong, C. H., Soeters, P. B., and Jalan, R. (2002) Interorgan ammonia metabolism in liver failure. *Neurochem. Int.* **41**, 177–188
13. Holecek, M., and Vodenicarovova, M. (2019) Effects of histidine load on ammonia, amino acid, and adenine nucleotide concentrations in rats. *Amino Acids* **51**, 1667–1680
14. Dam, G., Ott, P., Aagaard, N. K., and Vilstrup, H. (2013) Branched-chain amino acids and muscle ammonia detoxification in cirrhosis. *Metab. Brain Dis.* **28**, 217–220
15. Davuluri, G., Allawy, A., Thapaliya, S., Rennison, J. H., Singh, D., Kumar, A., Sandlers, Y., Van Wagoner, D. R., Flask, C. A., Hoppel, C., Kasumov, T., and Dasarathy, S. (2016) Hyperammonaemia-induced skeletal muscle mitochondrial dysfunction results in cataplerosis and oxidative stress. *J. Physiol.* **594**, 7341–7360
16. Lovell, J. T., Jenkins, J., Lowry, D. B., Mamidi, S., Sreedasyam, A., Weng, X., Barry, K., Bonnette, J., Campitelli, B., Daum, C., Gordon, S. P., Gould, B. A., Khasanova, A., Lipzen, A., MacQueen, A., *et al.* (2018) The genomic landscape of molecular responses to natural drought stress in Panicum hallii. *Nat. Commun.* **9**, 5213
17. Klemann, C., Martens, G. J. M., Sharma, M., Martens, M. B., Isacson, O., Gasser, T., Visser, J. E., and Poelmans, G. (2017) Integrated molecular landscape of Parkinson's disease. *NPJ Parkinsons Dis.* **3**, 14
18. Haider, S., and Pal, R. (2013) Integrated analysis of transcriptomic and proteomic data. *Curr. Genomics* **14**, 91–110
19. Schlotter, F., Halu, A., Goto, S., Blaser, M. C., Body, S. C., Lee, L. H., Higashi, H., DeLaughter, D. M., Hutcheson, J. D., Vyas, P., Pham, T., Rogers, M. A., Sharma, A., Seidman, C. E., Loscalzo, J., *et al.* (2018) Spatiotemporal multi-omics mapping generates a molecular atlas of the aortic valve and reveals networks driving disease. *Circulation* **138**, 377–393
20. Seliger, B., Dressler, S. P., Wang, E., Kellner, R., Recktenwald, C. V., Lottspeich, F., Marincola, F. M., Baumgartner, M., Atkins, D., and Lichtenfels, R. (2009) Combined analysis of transcriptome and proteome data as a tool for the identification of candidate biomarkers in renal cell carcinoma. *Proteomics* **9**, 1567–1581
21. Lau, E., Cao, Q., Lam, M. P. Y., Wang, J., Ng, D. C. M., Bleakley, B. J., Lee, J. M., Liem, D. A., Wang, D., Hermjakob, H., and Ping, P. (2018) Integrated omics dissection of proteome dynamics during cardiac remodeling. *Nat. Commun.* **9**, 120
22. Cisek, K., Krochmal, M., Klein, J., and Mischak, H. (2016) The application of multi-omics and systems biology to identify therapeutic targets in chronic kidney disease. *Nephrol. Dial. Transpl.* **31**, 2003–2011
23. Draghici, S., Khatri, P., Tarca, A. L., Amin, K., Done, A., Voichita, C., Georgescu, C., and Romero, R. (2007) A systems biology approach for pathway level analysis. *Genome Res.* **17**, 1537–1545
24. Robinson, S. W., Fernandes, M., and Husi, H. (2014) Current advances in systems and integrative biology. *Comput. Struct. Biotechnol. J.* **11**, 35–46
25. Kant, S., Davuluri, G., Alchirazi, K. A., Welch, N., Heit, C., Kumar, A., Gangadhariah, M., Kim, A., McMullen, M. R., Willard, B., Luse, D. S., Nagy, L. E., Vasiliou, V., Marini, A. M., Weiner, I. D., *et al.* (2019) Ethanol sensitizes skeletal muscle to ammonia-induced molecular perturbations. *J. Biol. Chem.* **294**, 7231–7244
26. Dasarathy, S., McCullough, A. J., Muc, S., Schneyer, A., Bennett, C. D., Dodig, M., and Kalhan, S. C. (2011) Sarcopenia associated with portosystemic shunting is reversed by follistatin. *J. Hepatol.* **54**, 915–921
27. Kitajima, S., Lee, K. L., Hikasa, H., Sun, W., Huang, R. Y., Yang, H., Matsunaga, S., Yamaguchi, T., Araki, M., Kato, H., and Poellinger, L. (2017) Hypoxia-inducible factor-1alpha promotes cell survival during ammonia stress response in ovarian cancer stem-like cells. *Oncotarget* **8**, 114481–114494
28. Kappler, M., Pabst, U., Rot, S., Taubert, H., Wichmann, H., Schubert, J., Bache, M., Weinholdt, C., Immel, U. D., Grosse, I., Vordermark, D., and Eckert, A. W. (2017) Normoxic accumulation of HIF1alpha is associated with glutaminolysis. *Clin. Oral Investig.* **21**, 211–224
29. Suzuki, H., Yanaka, A., Shibahara, T., Matsui, H., Nakahara, A., Tanaka, N., Muto, H., Momoi, T., and Uchiyama, Y. (2002) Ammonia-induced apoptosis is accelerated at higher pH in gastric surface mucous cells. *Am. J. Physiol. Gastrointest. Liver Physiol.* **283**, G986–G995
30. Jayakumar, A. R., Rama Rao, K. V., Tong, X. Y., and Norenberg, M. D. (2009) Calcium in the mechanism of ammonia-induced astrocyte swelling. *J. Neurochem.* **109 Suppl 1**, 252–257
31. Norenberg, M. D., Rama Rao, K. V., and Jayakumar, A. R. (2009) Signaling factors in the mechanism of ammonia neurotoxicity. *Metab. Brain Dis.* **24**, 103–117
32. Wang, F., Chen, S., Jiang, Y., Zhao, Y., Sun, L., Zheng, B., Chen, L., Liu, Z., Zheng, X., Yi, K., Li, C., and Zhou, X. (2018) Effects of ammonia on apoptosis and oxidative stress in bovine mammary epithelial cells. *Mutagenesis* **33**, 291–299
33. Borys, M. C., Linzer, D. I., and Papoutsakis, E. T. (1994) Ammonia affects the glycosylation patterns of recombinant mouse placental lactogen-I by Chinese hamster ovary cells in a pH-dependent manner. *Biotechnol. Bioeng.* **43**, 505–514
34. Yang, M., and Butler, M. (2000) Effect of ammonia on the glycosylation of human recombinant erythropoietin in culture. *Biotechnol. Prog.* **16**, 751–759

35. Gorg, B., Karababa, A., Shafigullina, A., Bidmon, H. J., and Haussinger, D. (2015) Ammonia-induced senescence in cultured rat astrocytes and in human cerebral cortex in hepatic encephalopathy. *Glia* **63**, 37–50
36. Welch, N., Attaway, A., Bellar, A., Alkhafaji, H., Vural, A., and Dasarathy, S. (2021) Compound sarcopenia in hospitalized patients with cirrhosis worsens outcomes with increasing age. *Nutrients* **13**, 659
37. Gleyzer, N., Vercauteren, K., and Scarpulla, R. C. (2005) Control of mitochondrial transcription specificity factors (TFB1M and TFB2M) by nuclear respiratory factors (NRF-1 and NRF-2) and PGC-1 family coactivators. *Mol. Cell. Biol.* **25**, 1354–1366
38. Evans, M. J., and Scarpulla, R. C. (1990) NRF-1: A trans-activator of nuclear-encoded respiratory genes in animal cells. *Genes Dev.* **4**, 1023–1034
39. Zhao, M., Chen, L., and Qu, H. (2016) CSGene: A literature-based database for cell senescence genes and its application to identify critical cell aging pathways and associated diseases. *Cell Death Dis.* **7**, e2053
40. Coppe, J. P., Desprez, P. Y., Krtolica, A., and Campisi, J. (2010) The senescence-associated secretory phenotype: The dark side of tumor suppression. *Annu. Rev. Pathol.* **5**, 99–118
41. Wang, R. S., Maron, B. A., and Loscalzo, J. (2015) Systems medicine: Evolution of systems biology from bench to bedside. *Wiley Interdiscip. Rev. Syst. Biol. Med.* **7**, 141–161
42. Schrattenholz, A., Groebe, K., and Soskic, V. (2010) Systems biology approaches and tools for analysis of interactomes and multi-target drugs. *Methods Mol. Biol.* **662**, 29–58
43. Ghazalpour, A., Bennett, B., Petyuk, V. A., Orozco, L., Hagopian, R., Mungrue, I. N., Farber, C. R., Sinsheimer, J., Kang, H. M., Furlotte, N., Park, C. C., Wen, P. Z., Brewer, H., Weitz, K., Camp, D. G., 2nd, *et al.* (2011) Comparative analysis of proteome and transcriptome variation in mouse. *PLoS Genet.* **7**, e1001393
44. Wang, D. (2008) Discrepancy between mRNA and protein abundance: Insight from information retrieval process in computers. *Comput. Biol. Chem.* **32**, 462–468
45. Kelly, R. T. (2020) Single-cell proteomics: Progress and prospects. *Mol. Cell. Proteomics* **19**, 1739–1748
46. Chen, G., Ning, B., and Shi, T. (2019) Single-cell RNA-seq technologies and related computational data analysis. *Front. Genet.* **10**, 317
47. Yuan, G. C., Cai, L., Elowitz, M., Enver, T., Fan, G., Guo, G., Irizarry, R., Kharchenko, P., Kim, J., Orkin, S., Quackenbush, J., Saadatpour, A., Schroeder, T., Shivdasani, R., and Tirosh, I. (2017) Challenges and emerging directions in single-cell analysis. *Genome Biol.* **18**, 84
48. Wang, Y., and Navin, N. E. (2015) Advances and applications of single-cell sequencing technologies. *Mol. Cell* **58**, 598–609
49. Rimland, C. A., Tilson, S. G., Morell, C. M., Tomaz, R. A., Lu, W. Y., Adams, S. E., Georgakopoulos, N., Otaizo-Carrasquero, F., Myers, T. G., Ferdinand, J. R., Gieseck, R. L., 3rd, Sampaziotis, F., Tysoe, O. C., Wesley, B., Muraro, D., *et al.* (2021) Regional differences in human biliary tissues and corresponding *in vitro* derived organoids. *Hepatology* **73**, 247–267
50. Tchoukalova, Y. D., Votruba, S. B., Tchkonia, T., Giorgadze, N., Kirkland, J. L., and Jensen, M. D. (2010) Regional differences in cellular mechanisms of adipose tissue gain with overfeeding. *Proc. Natl. Acad. Sci. U. S. A.* **107**, 18226–18231
51. Zhang, B., Zhou, Y., Lin, N., Lowdon, R. F., Hong, C., Nagarajan, R. P., Cheng, J. B., Li, D., Stevens, M., Lee, H. J., Xing, X., Zhou, J., Sundaram, V., Elliott, G., Gu, J., *et al.* (2013) Functional DNA methylation differences between tissues, cell types, and across individuals discovered using the M&M algorithm. *Genome Res.* **23**, 1522–1540
52. von Zglinicki, T., Wan, T., and Miwa, S. (2021) Senescence in post-mitotic cells: A driver of aging? *Antioxid. Redox Signal.* **34**, 308–323
53. Sapieha, P., and Mallette, F. A. (2018) Cellular senescence in postmitotic cells: Beyond growth arrest. *Trends Cell Biol.* **28**, 595–607
54. Kumar, A., Davuluri, G., Welch, N., Kim, A., Gangadhariah, M., Allawy, A., Priyadarshini, A., McMullen, M. R., Sandlers, Y., Willard, B., Hoppel, C. L., Nagy, L. E., and Dasarathy, S. (2019) Oxidative stress mediates ethanol-induced skeletal muscle mitochondrial dysfunction and dysregulated protein synthesis and autophagy. *Free Radic. Biol. Med.* **145**, 284–299
55. Singh, S. S., Kumar, A., Welch, N., Sekar, J., Mishra, S., Bellar, A., Gangadhariah, M., Attaway, A., Al Khafaji, H., Wu, X., Pathak, V., Agrawal, V., McMullen, M. R., Hornberger, T. A., Nagy, L. E., *et al.* (2021) Multiomics-identified intervention to restore ethanol-induced dysregulated proteostasis and secondary sarcopenia in alcoholic liver disease. *Cell. Physiol. Biochem.* **55**, 91–116
56. Tsien, C., Davuluri, G., Singh, D., Allawy, A., Ten Have, G. A., Thapaliya, S., Schulze, J. M., Barnes, D., McCullough, A. J., Engelen, M. P., Deutz, N. E., and Dasarathy, S. (2015) Metabolic and molecular responses to leucine-enriched branched chain amino acid supplementation in the skeletal muscle of alcoholic cirrhosis. *Hepatology* **61**, 2018–2029
57. Corces, M. R., Trevino, A. E., Hamilton, E. G., Greenside, P. G., Sinnott-Armstrong, N. A., Vesuna, S., Satpathy, A. T., Rubin, A. J., Montine, K. S., Wu, B., Kathiria, A., Cho, S. W., Mumbach, M. R., Carter, A. C., Kasowski, M., *et al.* (2017) An improved ATAC-seq protocol reduces background and enables interrogation of frozen tissues. *Nat. Methods* **14**, 959–962
58. Koster, J., and Rahmann, S. (2018) Snakemake-a scalable bioinformatics workflow engine. *Bioinformatics* **34**, 3600
59. Martin, M. (2011) Cutadapt removes adapter sequences from high-throughput sequencing reads. *EMBnet J.* **2011**, 3
60. Langmead, B., and Salzberg, S. L. (2012) Fast gapped-read alignment with Bowtie 2. *Nat. Methods* **9**, 357–359
61. Li, H., Handsaker, B., Wysoker, A., Fennell, T., Ruan, J., Homer, N., Marth, G., Abecasis, G., Durbin, R., and 1000 Genome Project Data Processing Subgroup (2009) The sequence alignment/map format and SAMtools. *Bioinformatics* **25**, 2078–2079
62. Quinlan, A. R., and Hall, I. M. (2010) BEDTools: A flexible suite of utilities for comparing genomic features. *Bioinformatics* **26**, 841–842
63. Zhang, Y., Liu, T., Meyer, C. A., Eeckhoute, J., Johnson, D. S., Bernstein, B. E., Nusbaum, C., Myers, R. M., Brown, M., Li, W., and Liu, X. S. (2008) Model-based analysis of ChIP-seq (MACS). *Genome Biol.* **9**, R137
64. Neph, S., Kuehn, M. S., Reynolds, A. P., Haugen, E., Thurman, R. E., Johnson, A. K., Rynes, E., Maurano, M. T., Vierstra, J., Thomas, S., Sandstrom, R., Humbert, R., and Stamatoyannopoulos, J. A. (2012) BEDOPS: High-performance genomic feature operations. *Bioinformatics* **28**, 1919–1920
65. Ewels, P., Magnusson, M., Lundin, S., and Kaller, M. (2016) MultiQC: Summarize analysis results for multiple tools and samples in a single report. *Bioinformatics* **32**, 3047–3048
66. Orchard, P., Kyono, Y., Hensley, J., Kitzman, J. O., and Parker, S. C. J. (2020) Quantification, dynamic visualization, and validation of bias in ATAC-seq data with ataqv. *Cell Syst.* **10**, 298–306.e294
67. McCarthy, D. J., Chen, Y., and Smyth, G. K. (2012) Differential expression analysis of multifactor RNA-Seq experiments with respect to biological variation. *Nucleic Acids Res.* **40**, 4288–4297
68. Cavalcante, R. G., and Sartor, M. A. (2017) annotatr: Genomic regions in context. *Bioinformatics* **33**, 2381–2383
69. Li, Z., Schulz, M. H., Look, T., Begemann, M., Zenke, M., and Costa, I. G. (2019) Identification of transcription factor binding sites using ATAC-seq. *Genome Biol.* **20**, 45
70. Khan, A., Fornes, O., Stigliani, A., Gheorghe, M., Castro-Mondragon, J. A., van der Lee, R., Bessy, A., Cheneby, J., Kulkarni, S. R., Tan, G., Baranasic, D., Arenillas, D. J., Sandelin, A., Vandepoele, K., Lenhard, B., *et al.* (2018) JASPAR 2018: Update of the open-access database of transcription factor binding profiles and its web framework. *Nucleic Acids Res.* **46**, D260–D266
71. Kim, D., Pertea, G., Trapnell, C., Pimentel, H., Kelley, R., and Salzberg, S. L. (2013) TopHat2: Accurate alignment of transcriptomes in the presence of insertions, deletions and gene fusions. *Genome Biol.* **14**, R36
72. Dobin, A., Davis, C. A., Schlesinger, F., Drenkow, J., Zaleski, C., Jha, S., Batut, P., Chaisson, M., and Gingeras, T. R. (2013) STAR: Ultrafast universal RNA-seq aligner. *Bioinformatics* **29**, 15–21
73. Anders, S., Pyl, P. T., and Huber, W. (2015) HTSeq–a Python framework to work with high-throughput sequencing data. *Bioinformatics* **31**, 166–169
74. Trapnell, C., Roberts, A., Goff, L., Pertea, G., Kim, D., Kelley, D. R., Pimentel, H., Salzberg, S. L., Rinn, J. L., and Pachter, L. (2012) Differential

gene and transcript expression analysis of RNA-seq experiments with TopHat and Cufflinks. *Nat. Protoc.* **7**, 562–578

75. Love, M. I., Huber, W., and Anders, S. (2014) Moderated estimation of fold change and dispersion for RNA-seq data with DESeq2. *Genome Biol.* **15**, 550
76. Mortazavi, A., Williams, B. A., McCue, K., Schaeffer, L., and Wold, B. (2008) Mapping and quantifying mammalian transcriptomes by RNA-Seq. *Nat. Methods* **5**, 621–628
77. Cox, J., Hein, M. Y., Luber, C. A., Paron, I., Nagaraj, N., and Mann, M. (2014) Accurate proteome-wide label-free quantification by delayed normalization and maximal peptide ratio extraction, termed MaxLFQ. *Mol. Cell. Proteomics* **13**, 2513–2526
78. Galili, T. (2015) dendextend: An R package for visualizing, adjusting and comparing trees of hierarchical clustering. *Bioinformatics* **31**, 3718–3720
79. Matys, V., Fricke, E., Geffers, R., Gossling, E., Haubrock, M., Hehl, R., Hornischer, K., Karas, D., Kel, A. E., Kel-Margoulis, O. V., Kloos, D. U., Land, S., Lewicki-Potapov, B., Michael, H., Munch, R., *et al.* (2003) TRANSFAC: Transcriptional regulation, from patterns to profiles. *Nucleic Acids Res.* **31**, 374–378
80. Raudvere, U., Kolberg, L., Kuzmin, I., Arak, T., Adler, P., Peterson, H., and Vilo, J. (2019) g:Profiler: A web server for functional enrichment analysis and conversions of gene lists (2019 update). *Nucleic Acids Res.* **47**, W191–W198
81. Schneider, C. A., Rasband, W. S., and Eliceiri, K. W. (2012) NIH image to ImageJ: 25 years of image analysis. *Nat. Methods* **9**, 671–675
82. Singh, K. D., Unal, H., Desnoyer, R., and Karnik, S. S. (2019) Mechanism of hormone peptide activation of a GPCR: Angiotensin II activated state of AT1R initiated by van der Waals attraction. *J. Chem. Inf. Model.* **59**, 373–385
83. Kramer, A., Green, J., Pollard, J., Jr., and Tugendreich, S. (2014) Causal analysis approaches in ingenuity pathway analysis. *Bioinformatics* **30**, 523–530
84. Perez-Riverol, Y., Csordas, A., Bai, J., Bernal-Llinares, M., Hewapathirana, S., Kundu, D. J., Inuganti, A., Griss, J., Mayer, G., Eisenacher, M., Perez, E., Uszkoreit, J., Pfeuffer, J., Sachsenberg, T., Yilmaz, S., *et al.* (2019) The PRIDE database and related tools and resources in 2019: Improving support for quantification data. *Nucleic Acids Res.* **47**, D442–D450